IV. INTERFEROGRAM ANALYSIS

10

Interferogram Analysis Overview

Interferogram Analysis Methods

Phase Calculation

Single Interferogram Techniques
(11)

Fringe-tracking methods
identifying fringe extrema
(11.2)

Fourier-transform
methods
(11.3)

choosing the
bandpass filter
(11.3.3)

Multiple Interferogram Techniques
Phase-Shifting Interferometry (PSI)
(12)

Simple algotithms
known phase step
(12.2)

Complex algotithms
unknown phase step
(12.5)

calculate phase steps
(12.5.2)

apply least-squares
(12.2.3)

Sort or Unwrap

Phase Unwrapping
(13)

Domain
Determination
(14a-d)

fringe contour
sorting/ordering
(11.2)

Simple/Filtered
methods
(13.2)

Path integral
methods
(*not covered*)

Fourier-Transform
Guided Unwrap
(13.5)

Wavefront Fitting
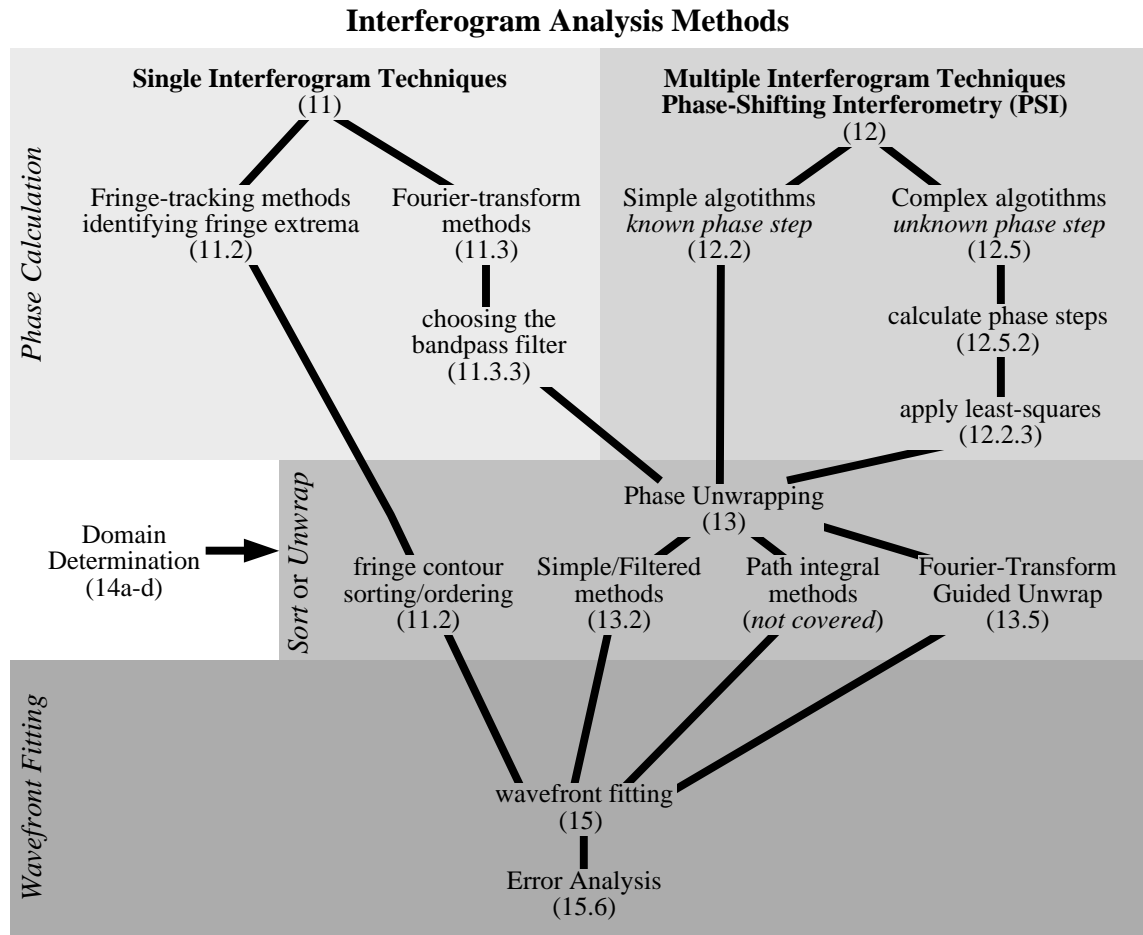
wavefront fitting
(15)

Error Analysis
(15.6)

Figure 1. Flowchart-outline of the interferogram analysis methods discussed in this dissertation. The chapter and section of each subject are shown in parentheses.

10. INTERFEROGRAM ANALYSIS OVERVIEW

"In any interferometric optical testing procedure the main objective is to determine the shape of the wavefront measured with respect to a best fit sphere." (Malacara and DeVore 1992)

Fundamentally, interferogram analysis is the solution of an inverse problem for which more than half of the information is missing and the data is coarsely sampled. An intensity *fringe pattern* is recorded at a location removed from the optical system under test, and the central question is, what electric field in the exit pupil produced the measured intensity distribution?

This section, comprised of Chapters 10 through 15, is dedicated to the practical solution of this inverse problem, with specific attention paid to interferogram analysis of EUV interferometric data. The goal is to retrieve the wavefront produced by the optical system under test. Following some simplifying assumptions, this difficult inverse problem becomes tractable and yields to rapid automated analysis methods.

Historically, methods for interferogram analysis have been divided into two main categories by their use of either single or multiple recorded interferogram images. Figure 1 outlines some of the available methods and shows in which section of this thesis they are discussed.

The *single interferogram analysis techniques* (Chapter 11) use either the fringe profiles or a Fourier-domain analysis of the intensity data to recover the phase. The *Fourier-transform method* is resistant to noise and can be highly efficient and very simple to apply. However, it suffers from low spatial-resolution and can be vulnerable to errors in the presence of abrupt features in the data.

Although more time-consuming and generally more challenging to implement than those involving a single interferogram, the *multiple interferogram techniques* (Chapter 12) combine several separate measurements to gain a significant statistical advantage. Utilizing the *temporal* domain of measurement by introducing a relative phase-shift between separate measurements, these Phase Shifting Interferometry (PSI) methods are able to achieve high accuracy *and* high spatial resolution. In the presence of imperfect data, however, the price paid for this higher resolution and accuracy is a significantly more difficult process of analysis, required to be robust in the presence of noise.

Once the phase is known, most analysis techniques require one further, critical step. Typically, the phase is only measured to within an integer multiple of 2π, and for each fringe in the interference pattern there can be an accompanying 2π discontinuity contour. To remove the presence of these discontinuities, the data must undergo a process called *phase unwrapping*. Although innocuous in appearance, the process of phase unwrapping (Chapter 13) is in itself a challenging inverse-problem and, in the opinion of the author, is the most difficult aspect of interferogram analysis. The literature is filled with phase unwrapping techniques for all occasions, and there appears to be little agreement as to the best approach.

After the wavefront phase has been successfully unwrapped, interpretation of the data often

requires that the measured surfaces be cast into a convenient set of orthogonal surface polynomials, such as the Zernike polynomials (Chapters 14 and 15). Once a coordinate system has been established for the data, the surface fitting can proceed in several ways, with some methods more appropriate for accurate analysis than others.

The procedures and techniques described in these chapters cover the process of interferogram analysis from start to finish, following several different paths. More than just a recitation of available methods, these chapters also introduce several novel procedures developed by the author, including the *Fourier-Transform Method of Phase-Shift Determination* (Chapter 12), developed to address difficulties with phase shift calibration, and the *Fourier-Transform Guided Unwrap Method* (Chapter 13), created and successfully employed to overcome significant high- and mid-spatial-frequency noise in the raw phase data. In addition, to facilitate accurate wavefront surface fitting and representation in terms of the aberration polynomials, an expedient Gram-Schmidt orthogonalization process (Chapter 15) is described.

11

Single Interferogram Analysis Methods

11.1 INTRODUCTION

Several methods of single-interferogram analysis are available when phase-shifting methods cannot be applied. Procedures that determine the positions of the fringe maxima or minima, or that utilize Fourier-domain processing, all rely on the same assumption: intensity variations caused by the *phase* of the test beam can be separated from those caused by the *amplitude* alone. Although this assumption makes these analysis methods highly sensitive to amplitude fluctuations that distort fringe positions, proper filtering of the interferogram data can greatly enhance the reliability of single interferogram analysis methods. This section provides a description of several of these methods and discusses their application.

The methods that scan the interferogram searching for local maxima, minima, or zero-crossings of the derivative are known as *fringe-tracking* or *fringe-center* techniques. Often the discrete derivative of the interferogram data is used to locate these contours of constant phase, each separated from the next by one wavelength. After the distinct phase contours are properly ordered, a (typically sparse) representation of the wavefront surface emerges. A wide variety of intensity-based fringe-tracking strategies are discussed by Yatagai (1993). In general, fringe-tracking methods suffer from non-uniform spatial sampling, and risk overlooking sub-wavelength variations in phase.

Since the advent of computer-aided data collection and image -processing in the last few decades, fringe-tracking techniques have become less widely used. Other techniques now offer significantly higher resolution and accuracy. Historically, however, the fringe-tracking methods have proven very successful, and thus merit a brief discussion here. These straightforward methods were applied at the earliest stages of this EUV interferometry research.

A separate class of procedures, the *Fourier-transform techniques,* utilize the spatial-frequency domain to separate low-to-mid spatial-frequency *phase* modulations of interest from lower-frequency *amplitude* modulations and high-frequency noise. Typically a spatial carrier-frequency is introduced to facilitate this Fourier-domain separation. The Fourier-transform method, first described by Takeda et al. (1981), has spawned a great number of adaptations and related techniques. The fundamental aspects of the Fourier-transform method are described in this chapter, with emphasis placed on the practical application of these methods to EUV interferometry.

11.1.1 *The Monotonic Phase Requirement*

Although the various fringe-tracking and Fourier-transform methods differ greatly in their approach and implementation, both types impose one important requirement on the measured wavefront phase.

> Proper analysis requires that *all* intensity maxima and minima represent points where the local phase is separated from other minima/maxima by an integral number of 2π cycles (or wavelengths, λ).
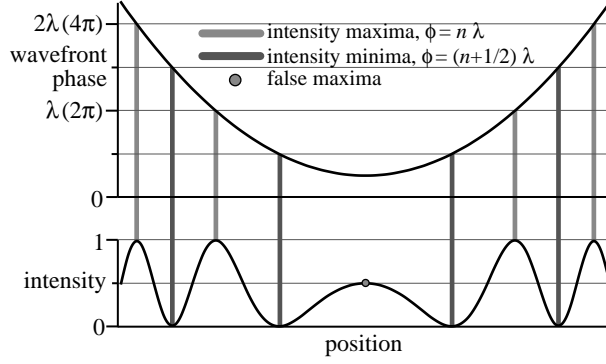
Figure 1. Interferogram intensity extrema occur when either of two conditions are met: the phase equals a multiple of $n\pi$ or the phase function itself reaches a maximum or minimum. To guarantee successful analysis, the singe interferogram techniques require that the latter case, illustrated by the central point of the graph, never occurs within the measurement domain. The figure shows the correspondence between each intensity extrema and the phase function.

This requirement removes potential ambiguities from the data. In some cases, filtering must be used to remove the isolated, spurious local maxima created by high-frequency noise. Excluding such noise, this rule applies mainly to low-spatial-frequency variations.

Consider Fig. 1, in which this requirement is violated and such phase ambiguity is illustrated. This figure is based on the one-dimensional expression

$$I(x) = A + B\cos[\phi(x)], \tag{1}$$

with $A = B = 1/2$ and a parabolic phase function. (This discussion can easily be extended to two dimensions, where a similar rule applies.) All but one of the local minima and maxima are seen to correspond to points where the phase crosses $\phi(x) = n\lambda/2$ waves (or $n\pi$ radians). Notice that in the center of the graph the local intensity maximum (indicated by a gray circle) corresponds to a local minima of the phase function, and *not* to a specific multiple of $\lambda/2$ in phase. Such a *false maximum* can confuse the fringe tracking analysis methods: it may be counted erroneously as a position where $\phi = n\lambda/2$ waves.

This requirement can be illustrated mathematically. From Eq. (1), the condition for an intensity extrema is

$$\frac{dI(x)}{dx} = 0 = -B\frac{d\phi(x)}{dx}\sin[\phi(x)]. \tag{2}$$

This condition is satisfied in two cases: first, where the phase function has a minimum or maximum

$$\frac{d\phi(x)}{dx} = 0, \tag{3}$$

and second, where the phase function crosses $n\pi$ radians, (or $n\lambda/2$ waves).

$$\sin[\phi(x)] = 0 \implies \phi(x) = n\pi \text{ [radians]} = \frac{n\lambda}{2} \text{ [waves]}. \tag{4}$$

In order to guarantee that over the measurement domain the *only* extrema come from $\phi(x)$ crossing $n\lambda/2$ waves, there must exist no point in the domain at which Eq. (3) is satisfied. This brings us to three *equivalent* requirements on $\phi(x)$.

> 1. $\phi(x)$ must not contain an extrema within the domain of measurement.
> 2. $\phi(x)$ must be *monotonic* within the measurement domain.
> 3. $d\phi(x)/dx \neq 0$ within the measurement domain. In two-dimensions, this requirement is $\nabla\phi \neq 0$.

A spatial carrier-frequency, or *tilt*, is introduced to satisfy this monotonic phase requirement. Beginning with a phase function $\phi_o(x)$ containing zero average slope, add or subtract a tilt component kx.

$$\phi(x) = \phi_o(x) - kx \,. \tag{5}$$

Using requirement 3 above, one statement of the monotonic phase requirement becomes

$$\frac{d\phi_o(x)}{dx} < k \,. \tag{6}$$

The test wavefront slope must neither equal nor exceed the slope of the carrier-frequency wave.

Experimentally, this places more of a requirement on the carrier-frequency than it does on the test wavefront. The carrier-frequency can usually be controlled to some extent, while the test wavefront is determined by the optical system being measured.

This slope restriction alone does *not* place a limitation on the highest measurable spatial-frequency of the test wavefront. In principle, high-frequency components of small phase amplitude *can* be measured as long as the slope does not exceed k. For example, if the phase function $\phi_o(x)$ contains a single spatial-frequency component k_A such that

$$\phi_o(x) = A\sin(k_A x) \tag{7}$$

then the limitation on the amplitude A imposed by Eq. (6) is

$$A < \frac{k}{k_A} \,. \tag{8}$$

In practice, there will be a wide range of spatial frequencies and amplitudes present in $\phi_o(x)$. This simplistic model requires that high-frequency components have smaller magnitude than the low-frequency components, to impose an upper limit on the phase *slope.*

The limitation on the highest allowable slope comes from the Nyquist limit (Nyquist 1928). In principle, the sampling density cannot be lower than two points per fringe or the pattern will be unmeasurable. The width of the detector elements may also contribute to a reduction in measurable fringe contrast if the fringe density is too high. There are sub-Nyquist interferometry (SNI) methods that rely on *a priori* wavefront information (Greivenkamp 1987).

11.2 APPLICATION OF THE FRINGE-TRACKING METHODS

This section is a brief digression into the application of fringe-tracking methods of interferogram fringe pattern analysis. These methods were used in the early stages of the EUV interferometry research,

applied only to the Fresnel zone plate measurements. (Once the more sophisticated Fourier-transform methods of single interferogram analysis were successfully implemented, they quickly replaced fringe-tracking.)

Assume, for the purposes of this discussion, that a spatial carrier-frequency has been introduced to generate a fringe pattern with a generally-horizontal fringe orientation. Contours of constant phase chosen for analysis may be those of the intensity *maxima*, the *minima*, or the so-called *zero-crossings*. The zero crossings are the inflection-point contours of the fringes.

One procedure for locating the fringe maxima uses the discrete derivative of the intensity along each column. Consider an interferogram $I(x, y)$ on a rectangular grid of size $N_x \times N_y$.

Procedure 1: Fringe-Tracking Method Using Fringe Maxima.

1. Loop i from 1 to N_x
2. $d(j) \equiv I(i, j+1) - I(i, j)$ *(single-column discreet derivative)*
3. $j^* \equiv \{j \mid d(j) \geq 0 \text{ AND } d(j+1) < 0\}$ *(set containing locations of the maxima)*
3a. $j^* \equiv \{j \mid d(j) \leq 0 \text{ AND } d(j+1) > 0\}$ *(alternately, the minima may be used)*
4. Add points $\{(i, j^*)\}$ to the set of maxima from which the contours are constructed.
4a. [Optional] Keep track of the *order* of these points vertically.
4b. [Optional] Use polynomial fitting of the neighboring points to more accurately locate the individual maxima, allowing the elements of j^* to take non-integral values.
5. Sort (order) the contour data into separate, "continuous" contours.

In Step 2, the maxima are identified as points where the derivative goes from non-negative to negative. Of course, noisy data can generate spurious maxima; the data may require filtering in the vertical direction. The median filter and various other low-pass filters have been recommended (Yatagai 1993).

Sorting the contour data means identifying the contour-line to which each maxima point belongs. This procedure is also called *fringe ordering*. When the contour lines are unbroken and span the width of the array, as is the case in Fig. 2(b), this exercise is almost trivial to perform. However, if the data exists on a limited sub-region, if contours are discontinuous, or if the contours deviate significantly from a pre-
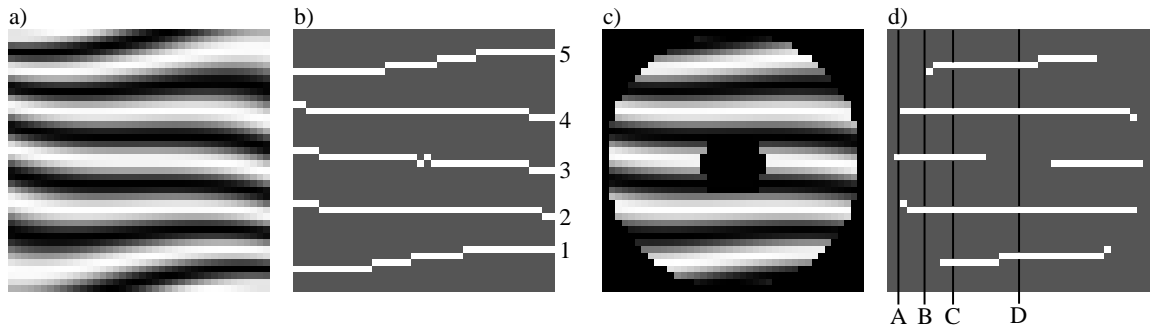

Figure 2. Illustration of the fringe-tracking method, with sorting. The vertical-direction derivative is used to locate the extrema of the interferograms in (a) and (c). The positions of these extrema, shown in (b) and (d), trace contours of constant path-length-difference between the two interfering beams. Each contour is separated from the next by one wavelength of path-length-difference. Analysis requires that each contour be regarded separately from its neighbors in a process known as *sorting*. Numbers indicate the index of the sorted contours. When the contours span the width of the domain, sorting by examination of the columns is trivial. However, when the domain does not reach the edges of the array or contains obstructions, automated sorting procedures become complex.

dictable direction, then the sorting algorithm may require a flexible approach. Fig. 2(d) shows a case where a flexible sorting routine is required. Notice here that scanning upward (or downward) along the columns indicated by the lines A, B, C, and D, a simple contour-counting algorithm would erroneously attribute adjacent maxima points to different contours. If the fringes do not reach the edge of the measurement domain, care must also be taken to avoid falsely attributing maxima or minima to points near the domain edges.

One severe limitation of the fringe-tracking techniques is the relative sparseness of the sampled wavefront contour data. If the fringe separation corresponds to N pixels on average in the detector measurement domain, then the coverage of the measurements is approximately $1/N$ of the total number of available points. Although this may be *thousands* of points, since those points are arranged along narrow stripes, the surface fitting and subsequent wavefront reconstruction may yield spurious wavefront curvature in regions not covered by the contours.

The decision on whether to use the maxima, minima, or zero-crossings depends on several competing factors. In the presence of noise, the signal-to-noise ratio is often highest at the peaks of the intensity pattern. Based on this alone, maxima location would appear to be more accurate than minima location. Complicating this assumption is the fact that variations of the background intensity or of the fringe amplitude can shift the locations of the extrema. These competing concerns must be addressed in choosing the best algorithm.

11.3 FOURIER-TRANSFORM METHODS

Since the early part of the 1980s, Fourier-transform techniques for interferogram fringe pattern analysis and wavefront recovery have gained widespread acceptance as the leading methods for single-interferogram analysis (Takeda et al. 1981, Nugent 1985, Bone et al. 1986, Kreis 1986, Roddier and Roddier 1987). In addition to their versatility and ease of application, the Fourier-transform techniques hold other, more significant advantages over the fringe-center methods. These Fourier methods often contain spatial-frequency filtering as one component of their application, and are thus more resistant to the presence of high-frequency noise, low-frequency background variation, and low-frequency fringe-amplitude variations. Furthermore, these methods generate wavefront data over the entire measurement domain, unlike the sparsely-sampling fringe-center methods.

In this thesis, Fourier-transform methods are used in the analysis of all of the Fresnel zoneplate data (Chapter 3) and for various measurements of the Schwarzschild objective where phase-shifting data is unavailable (Chapter 8).

The Fourier-transform methods are easily understood from consideration of the spatial-frequency-

spectrum of the interferogram data. To begin, the *real* one- or two-dimensional interferogram data is represented by additive and multiplicative intensity components. These components of the fringe modulation represent the stationary and the modulated intensity, respectively. As in the other single-interferogram techniques, a spatial carrier-frequency $\mathbf{k}_o$ is introduced to facilitate analysis.

$$I(\mathbf{r}) = A(\mathbf{r}) + B(\mathbf{r})\cos[\phi_o(\mathbf{r}) + \mathbf{k}_o \cdot \mathbf{r}], \quad \text{with } A, B, \phi_o \in R . \tag{9}$$

Successful implementation of the Fourier-transform techniques relies on frequency-domain separation of the interferogram *phase* modulation from the *amplitude* modulation. This requirement puts limitations on each term of the interferogram as represented in Eq. (9), and on the spatial carrier-frequency, as well. $A(\mathbf{r})$, $B(\mathbf{r})$, and $\phi(\mathbf{r})$ may contain both low- and high-frequency variations, but there must be a range of spatial frequencies over which these functions are *quiet* (arbitrarily small in magnitude). The spatial carrier-frequency is used to shift the phase-variations of interest into this *quiet* region of the domain. The range of phase modulation spatial frequencies that is available for accurate analysis is primarily determined by the spatial-frequency *width* of the quiet region.

Since the two terms in Eq. (9) are additive, it is always possible to attribute all of the high-frequency variations in the interferogram to $A(\mathbf{r})$ alone. (This is not true for phase-shifting analysis (Chapter 12), in which the stationary components are separable from the modulated components of the intensity.)

To facilitate the Fourier-domain representation of the interferogram, the cosine may be separated as follows.

$$I(\mathbf{r}) = A(\mathbf{r}) + \tfrac{1}{2} B(\mathbf{r}) e^{i[\phi_o(\mathbf{r}) + \mathbf{k}_o \cdot \mathbf{r}]} + \tfrac{1}{2} B(\mathbf{r}) e^{-i[\phi_o(\mathbf{r}) + \mathbf{k}_o \cdot \mathbf{r}]} , \tag{10}$$

$$I(\mathbf{r}) = A(\mathbf{r}) + C(\mathbf{r}) e^{i\mathbf{k}_o \cdot \mathbf{r}} + C^*(\mathbf{r}) e^{-i\mathbf{k}_o \cdot \mathbf{r}} , \tag{11}$$

where

$$C(\mathbf{r}) \equiv \tfrac{1}{2} B(\mathbf{r}) e^{i\phi_o(\mathbf{r})} \tag{12}$$

and * indicates the *complex conjugate*. From Eq. (11), the Fourier-transform of the interferogram may be written

$$i(\mathbf{k}) = a(\mathbf{k}) + c(\mathbf{k} - \mathbf{k}_o) + c^*(\mathbf{k} + \mathbf{k}_o) . \tag{13}$$

Here, functions denoted by upper case letters are used to indicate the *spatial* (measurement) domain, and lower-case letters denote the Fourier-transform of each. (The definition of the discrete Fourier-transform, as applied to interferogram data, is discussed in Section 11.3.2.) The phase information we seek is contained in $c(\mathbf{k} - \mathbf{k}_o)$, or equivalently in $c^*(\mathbf{k} + \mathbf{k}_o)$. The addition of the carrier-frequency facilitates the separation of either $c(\mathbf{k} - \mathbf{k}_o)$ or $c^*(\mathbf{k} + \mathbf{k}_o)$ from the other components of the spatial-frequency spectrum. $c(\mathbf{k} - \mathbf{k}_o)$ and $c^*(\mathbf{k} + \mathbf{k}_o)$ form separate *side-lobes* centered on $\mathbf{k}_o$ and $-\mathbf{k}_o$ respectively. The isolation of one side-lobe is our immediate goal.

Since $I(\mathbf{r})$ is real, its Fourier-transform $i(\mathbf{k})$ is *Hermitian*, indicating

$$i(\mathbf{k}) = i^*(-\mathbf{k}) . \tag{14}$$

The amplitude of the spatial-frequency spectrum $|i(\mathbf{k})|$ has polar symmetry about the central, zero-frequency component. $a(\mathbf{k})$ is also Hermitian and typically contains a strong peak near zero-frequency, related to the overall intensity of the recorded interferogram.

Depending on the phase aberrations present in the system under test, c and c^* typically consist of a narrow peak near zero-frequency. The presence of the carrier-frequency shifts c and c^* by $\mathbf{k}_o$ and $-\mathbf{k}_o$, respectively, where they can be isolated from the other spatial-frequency-domain components of the spectrum.

Applying to $i(\mathbf{k})$ a bandpass-filter centered about $\mathbf{k}_o$ (alternately, about $-\mathbf{k}_o$) in the spatial-frequency domain achieves several of our goals. One of the components $c(\mathbf{k} - \mathbf{k}_o)$ or $c^*(\mathbf{k} + \mathbf{k}_o)$ is isolated from the rest of the frequency spectrum. Symbolically,

$$i'(\mathbf{k}) \equiv Filtered_{\mathbf{k}_o}\{i(\mathbf{k})\} = Filtered_{\mathbf{k}_o}\{a(\mathbf{k}) + c(\mathbf{k} - \mathbf{k}_o) + c^*(\mathbf{k} + \mathbf{k}_o)\} \approx c(\mathbf{k} - \mathbf{k}_o). \tag{15}$$

Filtering destroys the Hermiticity of $i(\mathbf{k})$, and Fourier-inversion of $i'(\mathbf{k})$ produces an approximation to the complex function $C(\mathbf{r})$. $C(\mathbf{r})$ is only approximately known due to the necessary spatial-frequency-domain filtering and the possible overlap of $a(\mathbf{k})$ and $c^*(\mathbf{k})$. Filtering strategies are discussed in Section 11.3.3. Fourier-inversion of the filtered interferogram returns us to the spatial domain.

$$F^{-1}\{i'(\mathbf{k})\} \approx C(\mathbf{r})e^{i\mathbf{k}_o \cdot \mathbf{r}} = \tfrac{1}{2}B(\mathbf{r})e^{i\phi_o(\mathbf{r}) + i\mathbf{k}_o \cdot \mathbf{r}} . \tag{16}$$

The wavefront phase information is contained in the exponential term. Here there are several equivalent ways of determining $\phi_o(\mathbf{r})$.

$$\phi_o(\mathbf{r}) + \mathbf{k}_o \cdot \mathbf{r} = \tan^{-1}\left(\frac{\text{Im}\{C(\mathbf{r})\}}{\text{Re}\{C(\mathbf{r})\}}\right) = \tan^{-1}(\text{Im}\{C(\mathbf{r})\},\ \text{Re}\{C(\mathbf{r})\}) = \tan^{-1}[C(\mathbf{r})] , \tag{17a, b, c}$$

or, equivalently, $$\phi_o(\mathbf{r}) + \mathbf{k}_o \cdot \mathbf{r} = \text{Im}\{\ln[C(\mathbf{r})]\} . \tag{17d}$$

Note that the additive term $\mathbf{k}_o \cdot \mathbf{r}$ behaves simply as a removable wavefront *tilt* added to the phase function of interest. Regarding the arctangent, certain computer applications require the input arguments to be provided in one of the equivalent formats shown in Eqns. (17a) through (17c).

Since the arctangent and the complex logarithm are periodic functions, $\phi_o(\mathbf{r})$ is only determined to within a multiple of π or 2π. Equation (17a) returns $\phi_o(\mathbf{r})$ as a modulo π function, while Eqns. (17b) through (17d) return $\phi_o(\mathbf{r})$ modulo 2π. This common aspect of interferogram analysis leads to the necessity of *phase unwrapping* to remove the ambiguity caused by this loss of information, and to re-create a continuous wavefront. Phase unwrapping is the subject of Chapter 13.

Regarding the Fourier-inverse-transform of Eq. (16), Nugent (1985) recommends the optional step of *shifting* the filtered interferogram $i'(\mathbf{k})$ by $\pm\mathbf{k}_o$ to shift one of the symmetric $c(\mathbf{k})$ lobes to the zero-fre-

quency position *before* the inverse transform is performed. In so doing, the bandpass filter will be centered

on the zero-frequency, and all or most of the tilt will be removed. The difference here is mainly cosmetic. If

the carrier-frequency is precisely known, then $\phi_o(\mathbf{r})$ may be recovered directly from the methods of Eqns.

(17a) through (17d). When $\mathbf{k}_o$ is known only approximately, the shift in the spatial-frequency-domain

reduces the amount of wavefront tilt added to $\phi_o(\mathbf{r})$, and potentially eliminates a large number of wrap-

ping transitions caused by the modulo 2π reconstruction of $\phi_o(\mathbf{r})$.

Now that the mathematical framework has been established, the following two sections address issues

related to the practical application of the Fourier-transform method. The first section briefly discusses the dis-

crete Fourier-transform (DFT), and the second addresses the selection of the Fourier-domain filter used in the

Fourier-transform method.

11.3.1 *The Discrete Fourier-Transform*

Interferogram measurements are generally collected on a square-grid, discrete domain.

Consequently, all Fourier-transform operations required by the methods described in the previous section

are performed on this domain. In order to study the application of various Fourier-domain filters, we

begin with the conventional definition of the discrete Fourier-transform (DFT) (Conte and de Boor

1980:277-83). For an arbitrary function $G(\mathbf{r})$, with $\mathbf{r} \equiv (x, y)$, defined on the discrete, two-dimensional, N

$\times N$ domain, the Fourier-transform operation is defined as

$$F\{G(\mathbf{r})\} \equiv g(\mathbf{k}) \equiv \sum_{\substack{x=0 \\ y=0}}^{N-1} G(\mathbf{r}) \exp\left[\frac{i2\pi}{N}(\mathbf{k} \cdot \mathbf{r})\right], \tag{18}$$

or, equivalently, $$F\{G(x,y)\} \equiv g(k_x, k_y) \equiv \sum_{\substack{x=0 \\ y=0}}^{N-1} G(x,y) \exp\left[\frac{i2\pi}{N}(k_x x + k_y y)\right]. \tag{19}$$

Here, upper-case functions denote the spatial domain, while their lower-case counterparts refer to the

domain of spatial-frequencies. The position vector in the spatial-frequency domain $\mathbf{k}$ is defined in *cycles*.

The inverse transform is defined as

$$F^{-1}\{g(\mathbf{k})\} \equiv G(\mathbf{r}) \equiv \frac{1}{N^2} \sum_{\substack{k_x=0 \\ k_y=0}}^{N-1} g(\mathbf{k}) \exp\left[-\frac{i2\pi}{N}(\mathbf{k} \cdot \mathbf{r})\right], \tag{20}$$

with an analogous expression for $F^{-1}\{g(x, y)\}$. The coefficient $1/N^2$ in the definition of the inverse trans-

form guarantees that

$$F^{-1}\{F\{G(\mathbf{r})\}\} = G(\mathbf{r}). \tag{21}$$

Note: In many circumstances, computational efficiency is greatly enhanced by the application of the so-

called *fast Fourier-transform* (FFT). The FFT algorithm optimizes the computation of the discrete

Fourier-transform, although mathematically it is identical to the DFT.

11.3.2 *Analogy Between the Continuous Fourier-Transform and the DFT*

The DFT is actually a special case of the continuous Fourier-transform; considering it as such simplifies the description of filtering presented in the following section. For an arbitrary function $H(\mathbf{r})$ defined in the *x-y* plane, and periodic in *x* and *y* with period *N*, the Fourier transform of $H(\mathbf{r})$ is

$$F\{H(\mathbf{r})\} \equiv h(\mathbf{k}) \equiv \int\limits_{x=0}^{N} \int\limits_{y=0}^{N} H(\mathbf{r}) \exp\left[\frac{i2\pi}{N}(\mathbf{k}\cdot\mathbf{r})\right] d\mathbf{r} . \tag{22}$$

In the conventional definition, the argument of the exponential is $i\mathbf{k}\cdot\mathbf{r}$. Here, for analogy with the DFT case, the coefficient $2\pi/N$ has been extracted from $\mathbf{k}$, making $\mathbf{k}$ equivalent to $\boldsymbol{f}$ in the common definition.

The *comb* function helps to make the transition between the continuous and the discrete domains. The comb function may be defined in two similar ways:

$$\mathrm{comb}(x) \equiv \begin{cases} 1, & x \in Integers \\ 0, & \text{otherwise} \end{cases}, \quad \text{or} \ \ \mathrm{comb}(x) \equiv \sum_{n=-\infty}^{\infty} \delta(x-n) . \tag{23}$$

It is easily shown that the Fourier-transform of the comb function in one dimension is

$$F\{\mathrm{comb}(x)\} = \sum_{n=-\infty}^{\infty} \delta(k-n) . \tag{24}$$

Again, a comb function in the spatial-frequency domain. A direct analogy extends to two dimensions where

$$\mathrm{comb}(\mathbf{r}) \equiv \mathrm{comb}(x,y) \equiv \sum_{n_x=-\infty}^{\infty} \sum_{n_y=-\infty}^{\infty} \delta(x-n_x)\delta(y-n_y), \tag{25}$$

and
$$F\{\mathrm{comb}(\mathbf{r})\} \equiv \sum_{n_x=-\infty}^{\infty} \sum_{n_y=-\infty}^{\infty} \delta(k_x-n_x)\delta(k_y-n_y) . \tag{26}$$

When the comb function is included in the Fourier-transform, the continuous Fourier-transform integral reduces to the DFT summation in Eq. (18). By the Convolution Theorem (Goodman 1988:10), including the comb function with an arbitrary function in a continuous Fourier-transform produces the Fourier-transform of the arbitrary function, defined only at discrete positions. This important result enables us to simplify the discussion of bandpass and other filters applied within the Fourier-transform method of analysis: the discrete Fourier-transforms follow their continuous counterparts, but are defined only on a square-grid, discrete domain.

11.3.3 *Spatial-Frequency-Domain Filtering*

Extraction of phase information using the Fourier-transform methods of interferogram analysis requires the application of bandpass filters in the spatial-frequency domain. Selection of the *optimum* filter is a highly complicated process that may in fact require a case-by-case approach. However, several of the

most important filter characteristics can be identified and enumerated. This section defines general criteria for filter selection, and investigates the application of a Gaussian filter of arbitrary width.

11.3.3.1 *General Filter Requirements* Three general filter requirements are discussed in this section.

1. Side-lobe isolation.
2. Use of symmetric, real filter functions.
3. Smoothly varying filter amplitude (optional).

Define $t(\mathbf{k})$ as a filter function in the spatial-frequency domain. $T(\mathbf{r})$ and $t(\mathbf{k})$ are a corresponding Fourier-transform pair, with $T(\mathbf{r})$ defined in the spatial domain of measurement. The filter is applied by multiplying the spatial-frequency spectrum by the frequency-shifted filter function.

1. Side-lobe isolation. The foremost goal of the filter is to isolate one of the side-lobes of the spatial-frequency spectrum, containing $c(\mathbf{k}-\mathbf{k}_o)$, or $c^*(\mathbf{k}+\mathbf{k}_o)$, as described in Section 11.3. These symmetric lobes contain the phase information of interest. The magnitude and direction of the displacement is determined by the spatial carrier-frequency $\mathbf{k}_o$.

The minimum requirement for side-lobe isolation, recommended by some authors (Macy 1983, Kreis and Juptner 1989) is a simple *half-plane filter*, displaced slightly from the central frequency to transmit only one side-lobe. In this simple case, the high-frequency information (including noise) is preserved in the measured phase data.

A different approach is to transmit only a bounded region centered on one of the side-lobes. Examples of bounded filters are the *circular* (or *elliptical*) *top-hat* filter and the *Gaussian* filter, which, although technically *not* bounded, decays rapidly toward zero over a short distance from the side-lobe center. In the displacement direction (parallel to $\mathbf{k}_o$), the size is constrained by the separation of the side-lobe and central-lobe. This situation is *directly* analogous to the design considerations of the physical spatial filter window in the PS/PDI (Section 5.10). There is no such filter size constraint in the complementary (perpendicular) direction. In the $\mathbf{k}_o$ direction, the maximum allowable size is constrained by the width of the central lobe. Clearly, larger filter widths allow the transmission of relatively more high-spatial-frequency information; but to avoid overlap, filter radii larger than $|\mathbf{k}_o|/2$ should not be used. When measurements are primarily concerned with only the lowest spatial-frequency aberrations, a very *narrow* filter can be highly effective at significantly reducing noise.

When using a bounded filter function, the filter should be centered on the side-lobe peak (i.e. centered on $\pm\mathbf{k}_o$) to avoid *introducing* phase errors into the calculation. When $\mathbf{k}_o$ is not known in advance, it may be determined approximately by searching the spatial-frequency spectrum for a peak absolute value (or peak square-modulus), excluding from the search a small domain centered about the zero-frequency peak. Of course, since the spatial-frequency spectrum is Hermitian, there will be two peaks, one of which must be selected.

2. Use of symmetric, real functions. When selecting a filter, it is helpful to remember that the complex function of interest, $C(\mathbf{r})$ from Eq. (12), will be convolved with $T(\mathbf{r})$ by the filtering process. $t(\mathbf{k})$ must be carefully selected to ensure that $T(\mathbf{r})$ does not *introduce* phase effects into the data. Requiring $T(\mathbf{r})$ to be symmetric and real (except possibly for a leading complex constant) imposes the requirement that $t(\mathbf{k})$ also be symmetric and real. The simple half-plane filter described above is actually just a large rectangular window filter defined on the periodic domain and displaced from the central frequency. The top-hat and Gaussian filters are also symmetric filters displaced by $\pm\mathbf{k}_o$.

3. Smoothly varying amplitude. This optional requirement is imposed to reduce *ringing* introduced by the filtering process. Filters with sharp features (high slope, or discontinuities) in the spatial-frequency domain may *create* phase oscillations in the measurement. A discontinuity in $t(\mathbf{k})$, for example, may introduce alternating positive and negative lobes into $T(\mathbf{r})$ and, by convolution of $C(\mathbf{r})$ with these alternating lobes, cause ringing near any sharp feature in the data. Experience has shown that ringing plagues the use of both the half-plane (rectangular) filter and the top-hat filter. The Gaussian filter is a logical choice to eliminate the ringing problem: its transform is also Gaussian and contains no alternating lobes.

11.3.3.2 *The Gaussian Filter*

For this discussion, a Gaussian filter is defined in the continuous spatial-frequency domain in two dimensions as

$$t_G(\mathbf{k}) \equiv e^{-(\mathbf{k}/\kappa)^2} . \tag{27}$$

The radius κ at which the $1/e$ amplitude is reached is called the *width* of the filter. The two-dimensional Gaussian filter is separable into a product of two one-dimensional filters defined for any two perpendicular directions. A rotationally symmetric *circular* Gaussian filter, with two equivalent axes, may be defined. In other cases, it may be desirable to define an *elliptical* filter with two widths corresponding to the "semi-major" and "semi-minor" axes.

It is easily shown in one dimension that the continuous Fourier-inverse-transform of the Gaussian filter $t_G(k)$ is also Gaussian. Neglecting leading coefficients not important to this discussion, we have

$$t_G(k) \equiv \exp\left[-\left(\frac{k}{\kappa}\right)^2\right] \;\Rightarrow\; T_G(x) \propto \exp\left[-\left(\frac{x}{N/\pi\kappa}\right)^2\right]. \tag{28}$$

The width in the spatial domain $N/\pi\kappa$ is inversely related to the width in the spatial-frequency domain, as expected. This shows that a *narrow* Gaussian spatial-frequency-domain filter convolves the phase data with a *broad* Gaussian function and vice versa.

The application of circular Gaussian filters in the Fourier-transform method of interferogram analysis is illustrated in Fig. 3. Here, six filters of varying widths are separately used in the analysis of a simulated
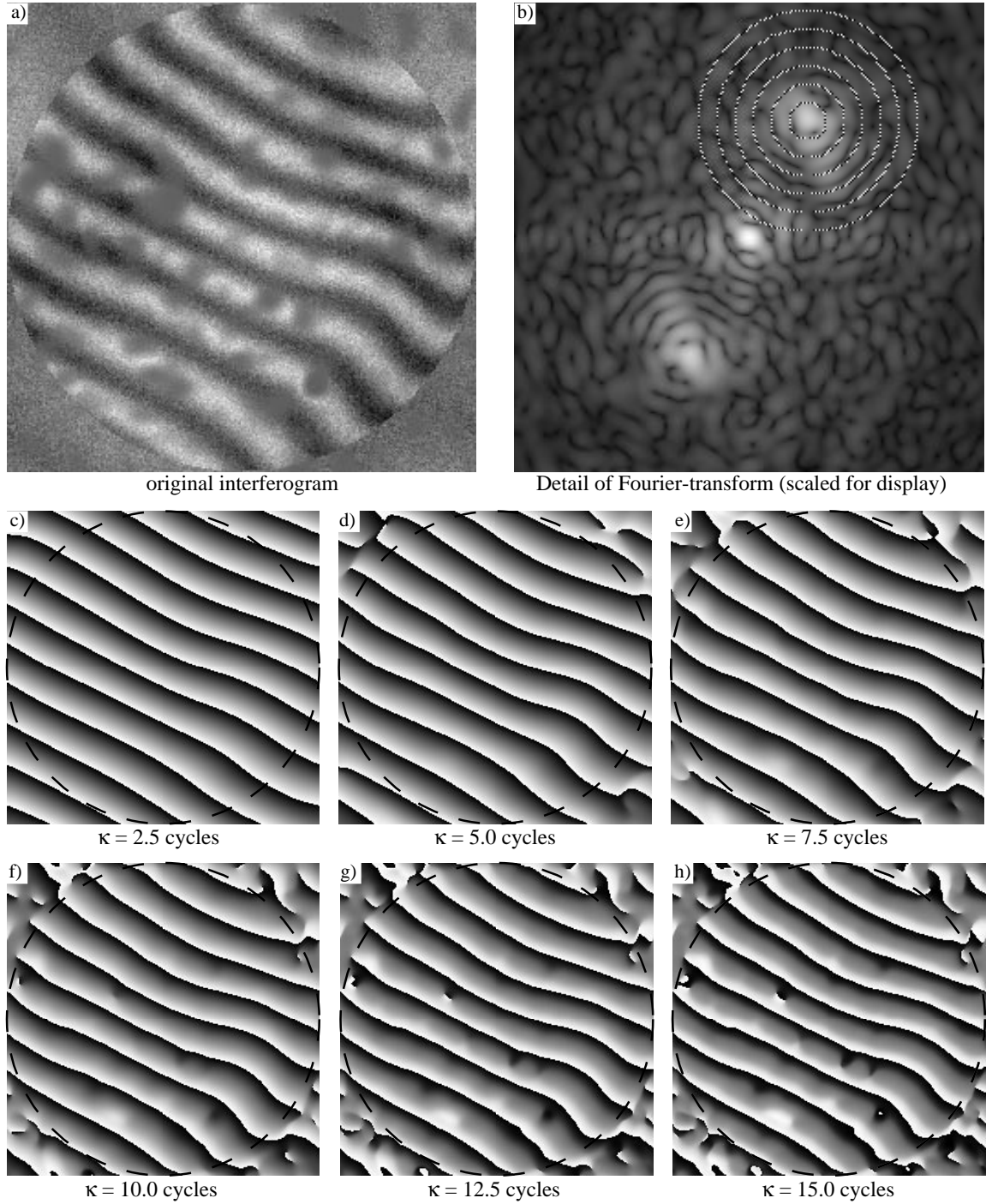
Figure 3. Illustration of the Fourier-transform method of single-interferogram phase-retrieval. The simulated interferogram (a) contains wavefront aberrations, noise, background variation, and blemishes. A Gaussian filter is applied to the spatial-frequency-spectrum (b) to isolate one of the side-lobes. Here, for purposes of illustration, six different filters of varying radius are used. The spectral width of the six filters is indicated by the concentric circles in (b). The modulo 2π phase functions are shown in (c) through (h) for each filter width. Notice that (c), at 2.5-cycles wide, is clearly *over-filtered*, while (g) and (h) are *under-filtered*, enabling the blemishes to cause serious phase errors that will complicate the unwrapping process.

interferogram pattern. The 256×256 pixel interference pattern contains numerous imperfections common to experimental data. The curvature of the fringes indicates imperfections in the underlying wavefront. Both high-frequency random noise and a low-frequency additive background intensity are present. To simulate blemishes in the test optic or on the detector, the interferogram is multiplied by a randomly-generated, high-contrast, mid-spatial-frequency pattern.

The interferogram is shown in Fig. 3(a) and a detail of the central portion of the spatial-frequency-spectrum is shown in 3(b), logarithmically scaled for display. The concentric dashed circles placed on the first-quadrant side-lobe of Fig. 3(b) indicate the widths of six different Gaussian filters used in the analysis. For each filter, the wrapped phasemap, calculated using the Fourier-transform method, is shown in Figs. 3(c) through 3(h).

The phase-discontinuities on the wrapped phasemaps follow the fringes closely over the circular measurement domain. Notice that in Figs. 3(c) through 3(e), where heavy filtering (a narrow filter) is applied, the mid-spatial-frequency blemishes and the high-frequency noise are effectively removed from the analysis. In 3(c), with the strongest filter, the calculated phase clearly fails to match the curvature of the wavefront seen in the raw fringe pattern. As the filter width is increased in 3(f) through 3(h), more frequency information is preserved. Effects related to the blemishes are first clearly visible in 3(f). In 3(g) and 3(h), the filtered region in the spatial-frequency domain begins to overlap both the central lobe and the side-lobe. Here, the phase-slope between the discontinuities appears to be non-linear. Also, the blemishes begin to create singular discontinuities in the phasemap. Observe the cusp created by the blemish just to the left of the image center. Such a cusp will create phase-unwrapping difficulties when the conventional phase-unwrapping methods are applied.

One procedure for the implementation of the Fourier-transform method of interferogram analysis, using a Gaussian filter, may now be outlined (Procedure 2). Begin with a square, $N \times N$ interferogram $I_o(x, y)$. The Gaussian filter here defined in Step 5 may be replaced by any other suitable filter. There are several nearly-equivalent representations of the arctangent application in Step 8. Alternatively, it may be represented by $\tan^{-1}\{\mathrm{Im}[I_1(x, y)], \mathrm{Re}[I_1(x, y)]\}$, $\tan^{-1}\{\mathrm{Im}[I_1(x, y)]/\mathrm{Re}[I_1(x, y)]\}$, or $\mathrm{Im}\{\log[I_1(x, y)]\}$.

Procedure 2: The Fourier-Transform Method

1. $f(i, j) \equiv F\{I_o(x, y)\}$ *(perform the FFT or DFT operation)*

2. $f_1(i, j) \equiv f(i, j) * \{1 - \exp[-(i^2 + j^2)/2^2]\}$ *(define a copy of the frequency spectrum; use a Gaussian filter to eliminate central lobe)*

3. $(i_m, j_m) \equiv$ location of maximum of $|f_1(i, j)|$ *(locate side-lobe peak: there are two, pick one)*

4. $\kappa \equiv 10$ *(define a Gaussian filter width κ. 10 cycles is arbitrary)*

5. $t_G(i, j) \equiv \exp[-(i^2 + j^2)/\kappa^2]$ *(define the Gaussian filter)*

6. $c(i, j) \equiv t_G(i - i_m, j - j_m) * f(i, j)$ *(to isolate one side-lobe, apply the filter, shifted to the location of the side-lobe maximum)*

7. $I_1(x, y) \equiv F^{-1}\{c(i, j)\}$ *(inverse transform)*

8. $\phi(x, y) \equiv \tan^{-1}\{I_1(x, y)\}$ *(determine phase)*

For clarity, Procedure 2 was written in an expanded form, with each term defined in a separate step. All of the steps may be combined into one *transform-filter-transform* representation, provided that the position of the side-lobe maximum is known in advance.

Procedure 2a: Concise Fourier-Transform Method

1. $\phi(x, y) \equiv \tan^{-1}\left[F^{-1}\left\{\exp\{-[(i-i_m)^2 + (j-j_m)^2]/\kappa^2\} * F\{I_o(x, y)\}\right\}\right]$

12

Phase-Shifting Interferometry

12.1 INTRODUCTION

The addition of computers and computer-controlled equipment into the fields of interferometry and optical testing opens the door to a new, powerful class of data-gathering and analysis methods known collectively as *Phase-Shifting Interferometry* (PSI). This chapter introduces some of the basic and extremely useful PSI algorithms and then describes a novel, versatile approach designed specifically to overcome limitations of the first implementation of the EUV PS/PDI described in this thesis.

Although highly effective in some instances, single-interferogram analysis methods are fraught with restrictions and limitations (Chapter 11). Because the single-interferogram techniques rely on the location of "fringe-centers," they are caught in a trade-off between precision and the desire for a high number of sampled data points. Most of these methods can only operate under conditions of high wavefront tilt, where the addition of a spatial-carrier-frequency is required to remove phase ambiguities. In other cases, the requirement is that there be no closed fringe contours. When only one interferogram is collected, additional information is required to determine the overall *sign* or *polarity* of the wavefront (i.e., concave or convex).

PSI overcomes many of the problems that plague single-interferogram analysis methods. PSI, which was first described by Carré in 1966 and fully developed in the 1970s (Crane 1969; Bruning et al. 1974; Wyant 1975), utilizes the *temporal domain* to collect a series of interferograms where only the reference phase of the interferometer is adjusted. Using the multiple interferograms, the wavefront phase is recovered at *each point* in the domain independently from its neighbors. The addition of a spatial-carrier-frequency is not required, the necessity of finding fringe-center locations is eliminated, and the wavefront polarity may be found unambiguously. Furthermore, using only the time-domain to find the phase at each point enhances the potential for high-spatial-frequency measurement. Unlike the single-interferogram techniques, PSI is capable of overcoming spatial variations in the detector response (sensitivity).

There are many available ways to implement the reference phase-shift required by PSI. One of the most common is by translation of a mirror in one arm of an Twyman-Green or Mach-Zender interferometer (Soobitsky 1986; Hayes 1989). The angle of a tilted, plane-parallel, transparent plate placed in the reference beam can be adjusted to induce a path-length change (Wyant and Shagam 1978). Alternatively, a small change of the optical frequency may be used in some cases to produce the required phase-change. The method used in the EUV PS/PDI is the translation of a grating through the beam of light, such that the diffracted beams acquire a phase-shift relative to the *undiffracted,* zeroth-order beam.

However the phase-shift is implemented, the analysis methods are similar. It is most convenient to describe the measured interferogram intensity with two terms: a *stationary* term and a *modulated* or *phase-dependent* term representing the fringes and their amplitude modulation.

198

$$I(\mathbf{r}, t) = A(\mathbf{r}) + B(\mathbf{r})\cos\left[\phi(\mathbf{r}) + \Delta(t)\right]. \tag{1}$$

In Eq. (1), the relative phase-shift between the test and reference beams is absorbed into the time-dependent term $\Delta(t)$. When a finite number of images are recorded, and the system is held stationary during measurement, the individual interferograms can be written as

$$I_n(\mathbf{r}) = A(\mathbf{r}) + B(\mathbf{r})\cos\left[\phi(\mathbf{r}) + \Delta_n\right] \tag{2}$$

The following sections of this chapter are dedicated to the phase-retrieval problem: finding $\phi(\mathbf{r})$ given a series of recorded interferograms. There are limitless varieties of phase-shifting algorithms tailored to meet the specific demands of a wide range of experimental conditions. As mentioned previously, each of these methods utilizes the *temporal* domain to achieve a relative phase shift between the test and reference waves while all other experimental conditions are held stable.

In principle, the analytic solution of Eq. (2) with its three unknowns requires that three or more interferograms be included in the analysis. In most cases, numerous solutions exist; considerable research has been dedicated to finding optimum methods of analysis in a variety of experimental conditions. A few of the most basic algorithms are presented here to demonstrate the available means of reducing experimental uncertainties. These methods, based on strict assumptions about the linear or non-linear phase-steps, are here referred to as the *simple techniques*. In contrast, the *complex techniques* presented in Section 12.4 make no such assumptions about the phase-shifts. The complex techniques are used exclusively in the analysis of phase-shifted EUV PS/PDI data described in this thesis.

12.2 SIMPLE PHASE-SHIFTING TECHNIQUES

Three of the simple phase-shifting techniques are presented in this section, followed by a comparison of their sensitivities to phase-shifting calibration errors. This discussion reveals how small refinements in the analysis can greatly improve the ability of these techniques to overcome some experimental limitations, specifically phase-shifting calibration errors. However, this discussion also illustrates the inadequacy of these methods when faced with large or unpredictable calibration errors. The sections on the complex phase-shifting techniques address these issues.

12.2.1 *The Four-Step Algorithm*

The *four-step algorithm* (Greivenkamp and Bruning 1992:510-513) is a good place to begin the discussion of PSI analysis methods, because among available algorithms it is perhaps easiest to understand. Assume that four interferograms are collected with a relative phase-step of $\pi/2$ between each. The four interferograms may be expressed as

$$
\begin{aligned}
I_1(\mathbf{x}) &= A(\mathbf{x}) + B(\mathbf{x})\cos[\phi(\mathbf{x})] & &= A(\mathbf{x}) + B(\mathbf{x})\cos[\phi(\mathbf{x})] \\
I_2(\mathbf{x}) &= A(\mathbf{x}) + B(\mathbf{x})\cos\left[\phi(\mathbf{x}) + \tfrac{\pi}{2}\right] & &= A(\mathbf{x}) - B(\mathbf{x})\sin[\phi(\mathbf{x})] \\
I_3(\mathbf{x}) &= A(\mathbf{x}) + B(\mathbf{x})\cos[\phi(\mathbf{x}) + \pi] & &= A(\mathbf{x}) - B(\mathbf{x})\cos[\phi(\mathbf{x})] \\
I_4(\mathbf{x}) &= A(\mathbf{x}) + B(\mathbf{x})\cos\left[\phi(\mathbf{x}) + \tfrac{3\pi}{2}\right] & &= A(\mathbf{x}) + B(\mathbf{x})\sin[\phi(\mathbf{x})]
\end{aligned}
\tag{3}
$$

Extracting $\phi(x)$ from the set of measurements above is straightforward. One analytic solution is

$$
\phi(\mathbf{x}) = \tan^{-1}\left[\frac{I_4 - I_2}{I_1 - I_3}\right], \quad \text{or } \phi(\mathbf{x}) = \tan^{-1}(I_4 - I_2, I_1 - I_3).
\tag{4}
$$

For clarity, the spatial dependence of the interferograms I_n is implied, but not written explicitly here. Notice that subtraction within both the numerator and denominator removes the stationary, additive component $A(x)$, while division eliminates the multiplicative term $B(x)$. In this way, $\phi(x)$ modulo 2π, or $\phi(x)$ modulo π is obtained.

Often the *fringe modulation* or *fringe contrast* is of interest. Here, $\gamma(x)$ is defined as the ratio of the amplitude of the modulated intensity to the (temporal-domain) average intensity at a given point $\mathbf{x}$.

$$
\gamma(\mathbf{x}) \equiv \frac{B(\mathbf{x})}{A(\mathbf{x})}.
\tag{5}
$$

It can be shown that in the Four-Step algorithm, the modulation is

$$
\gamma(\mathbf{x}) = \frac{2\sqrt{(I_4 - I_2)^2 + (I_1 - I_3)^2}}{I_1 + I_2 + I_3 + I_4}.
\tag{6}
$$

12.2.2 The Hariharan Five-Step Algorithm

When more than three phase-shifted interferograms are collected, there exist multiple ways available to extract $\phi(x)$ from the data analytically. The *Hariharan algorithm* for five steps (Hariharan 1987) in particular, chooses a solution with reduced sensitivity to phase-shift calibration errors. (Error analysis is discussed in Section 12.3.) The Hariharan method uses five images with a linear, relative phase-step α between frames. Define Δ as a vector of phase-step values.

$$
\Delta = (-2\alpha,\ -\alpha,\ 0,\ \alpha,\ 2\alpha),
\tag{7}
$$

$$
\begin{aligned}
I_1(\mathbf{x}) &= A(\mathbf{x}) + B(\mathbf{x})\cos[\phi(\mathbf{x}) + \Delta_1] & &= A(\mathbf{x}) + B(\mathbf{x})[\cos\phi(\mathbf{x})\cos 2\alpha + \sin\phi(\mathbf{x})\sin 2\alpha] \\
I_2(\mathbf{x}) &= A(\mathbf{x}) + B(\mathbf{x})\cos[\phi(\mathbf{x}) + \Delta_2] & &= A(\mathbf{x}) + B(\mathbf{x})[\cos\phi(\mathbf{x})\cos 2\alpha + \sin\phi(\mathbf{x})\sin 2\alpha] \\
I_3(\mathbf{x}) &= A(\mathbf{x}) + B(\mathbf{x})\cos[\phi(\mathbf{x}) + \Delta_3] & &= A(\mathbf{x}) + B(\mathbf{x})\cos\phi(\mathbf{x}) \\
I_4(\mathbf{x}) &= A(\mathbf{x}) + B(\mathbf{x})\cos[\phi(\mathbf{x}) + \Delta_4] & &= A(\mathbf{x}) + B(\mathbf{x})[\cos\phi(\mathbf{x})\cos\alpha - \sin\phi(\mathbf{x})\sin\alpha] \\
I_5(\mathbf{x}) &= A(\mathbf{x}) + B(\mathbf{x})\cos[\phi(\mathbf{x}) + \Delta_5] & &= A(\mathbf{x}) + B(\mathbf{x})[\cos\phi(\mathbf{x})\cos 2\alpha - \sin\phi(\mathbf{x})\sin 2\alpha]
\end{aligned}
\tag{8}
$$

These expressions are combined to form

$$
\tan\phi(\mathbf{x}) = \frac{2\sin\alpha\,(I_2 - I_4)}{2I_3 - I_5 - I_1}.
\tag{9}
$$

The optimum choice of α occurs where the method is least sensitive to errors in α. Differentiating the right-hand-side of Eq. (9) with respect to α, it is easily shown that the minimum of the derivative occurs where $\alpha = \pi/2$. With this quarter-cycle phase-step, the phase and modulation expressions are

$$\phi(\mathbf{x}) = \tan^{-1}\left[\frac{2(I_2 - I_4)}{2I_3 - I_5 - I_1}\right], \quad \text{or} \quad \phi(\mathbf{x}) = \tan^{-1}\left[2(I_2 - I_4), 2I_3 - I_5 - I_1\right], \tag{10}$$

and

$$\gamma(\mathbf{x}) = \frac{3\sqrt{4(I_4 - I_2)^2 + (I_1 + I_5 - 2I_3)^2}}{2(I_1 + I_2 + 2I_3 + I_4 + I_5)}. \tag{11}$$

With $\alpha = \pi/2$, the first and last interferograms are nominally the same. However, to preserve the insensitivity to calibration errors, this assumption is not imposed in the analysis. Notice again that subtraction within the numerator and denominator removes the additive term, while the division eliminates the multiplicative term.

12.2.3 *The Least-Squares Algorithm*

One pragmatic approach is the *least-squares algorithm* (Bruning et al. 1974, Greivenkamp 1984), in which $N \geq 3$ interferograms are combined using arbitrary, known phase-shifts. Although this method is not optimized against linear phase-shift calibration errors in the same way that other methods are, by allowing arbitrary phase-steps it proves to be the most versatile of the phase-shifting analysis algorithms described here. This versatility will be utilized by the complex techniques described in Section 12.4.

When the phase-shifts are known by some external means, application of this method is straightforward. For N measured interferograms, the phase-steps are

$$\mathbf{\Delta} = (\Delta_1, \Delta_2, \ldots, \Delta_N). \tag{13}$$

The n-th interferogram may be written in the conventional way, and then expanded as follows:

$$I_n(\mathbf{x}) = A(\mathbf{x}) + B(\mathbf{x})\cos[\phi(\mathbf{x}) + \Delta_n] = a_0(\mathbf{x}) + a_1(\mathbf{x})\cos\Delta_n + a_2(\mathbf{x})\sin\Delta_n. \tag{13}$$

Here, the phase-steps Δ_n have been separated from the unknown phase $\phi(x)$ using the definitions

$$\begin{cases} a_0(\mathbf{x}) \equiv A(\mathbf{x}) \\ a_1(\mathbf{x}) \equiv B(\mathbf{x})\cos\phi(\mathbf{x}) \\ a_2(\mathbf{x}) \equiv -B(\mathbf{x})\sin\phi(\mathbf{x}) \end{cases}. \tag{14}$$

These are the three unknowns for which we must solve. Since the phase-steps are known, the $\sin\Delta_i$ and $\cos\Delta_i$ terms are simply the scalar coefficients of the unknown $a_1(x)$ and $a_2(x)$ in Eq. 13, and are identical for all points x in the measurement domain.

Applying the method of least-squares separately at each point x_i of $\mathbf{x}$, the goal is to minimize the *error function* $E^2(x_i)$, defined as

$$E_i^2 \equiv E^2(x_i) \equiv \sum_{n=1}^{N} \left[I_n(x_i) - a_0(x_i) - a_1(x_i)\cos\Delta_n - a_2(x_i)\sin\Delta_n \right]^2 . \tag{15}$$

The error function is related to the *fit variance*, where it is assumed that each measurement $I_i(x_i)$ contains the same uncertainty.

At each x_i, $E^2(x_i)$ is minimized by differentiating Eq. (15) with respect to the three unknowns a_0, a_1, and a_2. The resultant expression may be written in matrix form

$$\begin{bmatrix} N & \Sigma\cos\Delta_n & \Sigma\sin\Delta_n \\ \Sigma\cos\Delta_n & \Sigma\cos^2\Delta_n & \Sigma\cos\Delta_n\sin\Delta_n \\ \Sigma\sin\Delta_n & \Sigma\cos\Delta_n\sin\Delta_n & \Sigma\sin^2\Delta_n \end{bmatrix} \begin{bmatrix} a_0(x_i) \\ a_1(x_i) \\ a_2(x_i) \end{bmatrix} = \begin{bmatrix} \Sigma I_n(x_i) \\ \Sigma I_n(x_i)\cos\Delta_n \\ \Sigma I_n(x_i)\sin\Delta_n \end{bmatrix}, \tag{16a}$$

$$A(\Delta)\mathbf{a}(x_i) = \mathbf{b}(x_i, \Delta) . \tag{16b}$$

Here, Σ is a shorthand notation representing the sum over the N measurements, with n as the summation index. The symmetric matrix $\mathbf{A}(\Delta)$, called the *curvature matrix*, depends only on the known phase-shifts, while the vector $\mathbf{b}(x_i, \Delta)$ contains the measured interferogram data. $\mathbf{A}(\Delta)$ may be calculated just once, yet the calculation of $\mathbf{b}(x_i, \Delta)$ must be done separately at every point in the measurement domain. The solution for the coefficient vector $\mathbf{a}(x_i)$ requires inverting $\mathbf{A}(\Delta)$, and pre-multiplying both sides of Eq. (16b).

$$\mathbf{a}(x_i) = A^{-1}(\Delta)\mathbf{b}(x_i, \Delta) \tag{17}$$

When there are three or more unique phase steps, the rows will be independent and $\mathbf{A}(\Delta)$ will be invertible. Once $\mathbf{a}(x_i)$ is known, the phase $\phi(x_i)$ and modulation $\gamma(x_i)$ are easily found. Over the whole domain,

$$\phi(\mathbf{x}) = \tan^{-1}\left[\frac{-a_2(\mathbf{x})}{a_1(\mathbf{x})} \right], \quad \text{or} \quad \phi(\mathbf{x}) = \tan^{-1}\left[-a_2(\mathbf{x}), a_1(\mathbf{x}) \right], \tag{18}$$

and

$$\gamma(\mathbf{x}) \equiv \frac{\sqrt{a_1^2(\mathbf{x}) + a_2^2(\mathbf{x})}}{a_0(\mathbf{x})} . \tag{19}$$

The sensitivity of the least-squares method with $\pi/2$ phase steps is discussed in Section 8.10.4.

12.3 LINEAR PHASE-SHIFTING CALIBRATION ERRORS AND THE SIMPLE ALGORITHMS

One important source of measurement errors facing every type of phase-shifting analysis is phase-step calibration errors. Any means used to generate the relative phase-shift is vulnerable to errors in the step-increments induced by inaccuracies, non-linearities, and random noise in the components. For instance, a stage that is perfectly repeatable and linear may be mis-calibrated by several percent; a stage driven over relatively long distances by piezoelectric transducers may exhibit non-linearities; and the finite precision of translation stages may introduce random errors into the positioning.

Many of the simple analysis techniques attempt to compensate for and reduce sensitivity to phase-shifting errors in a number of ways. When the phase-errors are small, the phase-shift may be modeled using a power-series expansion about their intended values. The first-order model describes the ideal phase-shift, plus a linear error. Note that the phase *step* or phase *increment* is simply the discrete derivative of the phase itself. Thus, an error that is *linear* in phase is equivalent to a *constant* offset (calibration error) in the step.

Consider the effects of a linear phase calibration error on the simple algorithms described in Section 12.2. Here, assume that the experimental phase-increment α' is related to the *target* phase increment α by a constant offset ε.

$$\alpha' = \alpha + \varepsilon, \tag{20}$$

making the phase steps

$$\mathbf{\Delta} = (0, \alpha', 2\alpha', \ldots, n\alpha', \ldots) = (0, \alpha + \varepsilon, 2\alpha + 2\varepsilon, \ldots, n\alpha + n\varepsilon, \ldots). \tag{21}$$

"Propagating" the small error ε through the Four-Step algorithm with $\alpha = \pi/2$ yields a phase error $\Delta\phi' \equiv (\phi' - \phi - \text{constant})$ of

Four-Step algorithm: $\qquad \Delta\phi' = \frac{1}{2}\cos(2\phi)\varepsilon - \frac{1}{8}\sin(4\phi)\varepsilon^2 + O[\varepsilon^3]$. $\hfill (22)$

Notice that the phase error is periodic in multiples of ϕ and has first-order dependence on ε. This commonly observed behavior is called *fringe print-through* because the fringe pattern (or harmonics of it) are visible in the phasemap. (Section 8.10.4 gives an experimental example of fringe print-through.) A constant phase term with ε-dependence was removed from Eq. (2) because it depends only on a constant offset in the phase-step definition.

Similar analysis conducted on the Hariharan algorithm shows a very different result.

Hariharan algorithm: $\qquad \Delta\phi' = \frac{1}{4}\sin(2\phi)\varepsilon^2 + O[\varepsilon^4]$. $\hfill (23)$

While again the error is periodic in multiples of ϕ, the dependence on the phase-step error ε has now been reduced to second-order. This dependence is illustrated in Fig. 1. The collection of one additional interferogram (five instead of four) has improved the uncertainty of the phase recovery significantly.

Note on Print-through. The significance of fringe print-through depends on several factors, including the amplitude and spatial-frequency of the error term $\Delta\phi'$. From the two examples presented, it is clear that the spatial-frequency of the print-through is related to harmonics of the fringe period. When high fringe density makes the spatial-frequency of the print-through much higher than the low-spatial-frequency of the aberrations of interest, then the print-through errors average to zero over a typical length scale. In that case the significance of fringe print-through is greatly reduced. Unfortunately, this averaging cannot occur for low fringe densities. Hence print-through can be a very serious problem, and great care
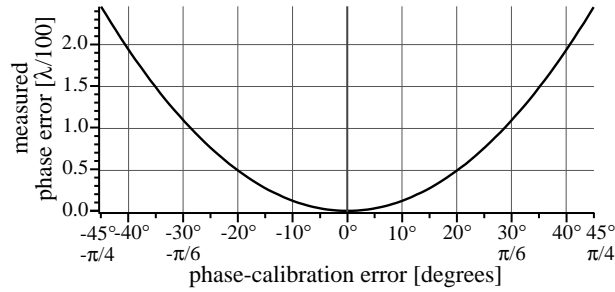
Figure 1. The effect of phase-step calibration errors on the Hariharan method of phase-retrieval. Designed to reduce sensitivity to calibration errors, the Hariharan method shows a maximum error of approximately 0.01 λ (waves) for calibration errors below 30° per step. Not shown in this figure is the periodic dependence of the measurement error on the wavefront phase.

must be taken to eliminate it. Section 8.10.2 reports experimental observation and elimination of fringe print-through with EUV PS/PDI data.

Numerous phase-shifting analysis techniques have been developed to reduce sensitivity to linear phase-step calibration errors (Creath 1986, Schmit and Creath 1992). Still other methods seek higher accuracy by modeling non-linear phase-increments (de Groot 1995). Analysis in the temporal domain provides insight into the behavior and facilitates the development of these advanced methods. By utilizing more phase-steps, and by finding alternate analytical solutions, the number of possible phase-recovery techniques is truly limitless.

Aside from the expense in time, collecting increasing numbers of interferograms for analysis is beneficial in virtually all circumstances. In addition to the potential for compensation of the effects of phase-calibration errors, having more data helps reduces sensitivity to noise. However, regarding phase-step calibration errors, each additional phase-step introduces one more degree of freedom. In principle, it requires a polynomial of order $(N-1)$ to model the behavior of N arbitrary phase steps. Given N interferograms, and N unknown phase-steps, we are faced with a system of $N+3$ variables, but only N equations (A, B, and ϕ are the extra three variables).

This is where the simplified models of the phase-step errors becomes necessary. For small phase-step errors and carefully chosen phase-retrieval algorithms, fringe print-through can be minimized. However, if the phase errors are large and unpredictable, then adding more interferograms to the analysis may not overcome the problem. EUV interferometry of the 10× Schwarzschild objective, described in this thesis, was faced with the latter circumstance; a different approach, capable of utilizing data collected with irregular phase-increments was required. A novel method, developed by the author to meet these needs, is presented in Section 12.5.2.

12.4 COMPLEX PHASE-SHIFTING TECHNIQUES

The simple phase-shifting techniques impose a linear or non-linear phase-step model on the data analysis. Optimization of these methods proceeds from the point of view that the incremental collection of

more interferograms enables the compensation of more non-linear phase-shifting effects. However, as stated previously, when the phase-shift errors are large and unpredictable, the inclusion of more phase-steps may not improve the analysis. This latter, difficult experimental circumstance arose in the EUV PS/PDI research, and prompted the author to develop a complex phase-shifting technique that has been implemented with great success.

Due to the limitations of the translation stages used to position the grating beam-splitter/phase-shifting element, the phase-shifting steps were neither linear nor predictable. Errors as large as 0.04 cycles, or 16% of the target $\pi/2$ phase increment, were routinely observed. Analysis using the simple techniques is compromised by the presence of significant fringe-print-through (Section 8.10.4).

A separate approach to interferogram analysis in the presence of high phase-shift uncertainty is to use the available data to determine the *phase-steps* themselves prior to or concurrently with the analysis of the phase at each point. One stated advantage of the phase-shifting algorithms is their individual treatment of each point in the measurement domain. Yet, while the phase function $\phi(\mathbf{x})$ is local, the phase-steps $\mathbf{\Delta}$ are global and in principle affect all measurement points equally. Determination of the phase-steps must be possible.

Formulated, as before, with N interferograms, and N *unknown* phase steps $\mathbf{\Delta}$,

$$\mathbf{\Delta} = \left(\Delta_1, \Delta_2, \cdots, \Delta_N\right),\tag{24}$$

and the *n*-th interferogram is written as

$$I_n(\mathbf{x}) = A(\mathbf{x}) + B(\mathbf{x})\cos\left[\phi(\mathbf{x}) + \Delta_n\right].\tag{25}$$

At each domain point, there is a set of N equations, with $N + 3$ unknowns (A, B, ϕ, and $\Delta_1, \ldots, \Delta_N$), making direct solution impossible. However, by utilizing all or a subset of the domain points (there are often hundreds of thousands), there exist a number of available strategies for determining $\mathbf{\Delta}$. Determining $\mathbf{\Delta}$ is the key to the complex phase-shifting techniques. Once $\mathbf{\Delta}$ is known, application of the least-squares algorithm to recover the phase $\phi(\mathbf{x})$ is trivial.

12.4.1 *Global Least-Squares*

One iterative method, described by Han and Kim (1994), seeks to minimize a global error function with respect to the three unknowns at each point, and the N phase-shifts. Following the least-squares algorithm of Section 12.2.3, the error function is defined individually for each domain point as

$$E_i^2 \equiv E^2(x_i) \equiv \sum_{n=1}^{N}\left[I_n(x_i) - a_0(x_i) - a_1(x_i)\cos\Delta_n - a_2(x_i)\sin\Delta_n\right]^2.\tag{26}$$

Now, allowing the phase steps Δ_n to be chosen freely, a *global error function E^2* takes the form

$$E^2(\mathbf{\Delta}, \mathbf{x}) \equiv \sum_{i=0}^{N_i} E_i^2 = \sum_{i=0}^{N_i} \sum_{n=1}^{N} \left[I_n(x_i) - a_0(x_i) - a_1(x_i) \cos\Delta_n - a_2(x_i) \sin\Delta_n \right]^2 . \qquad (27)$$

Here N_i is the number of domain points used in this calculation. Because the phase steps Δ_n appear as the arguments of cosine and sine in Eq. (27), solution will require a *non-linear least-squares* approach. For any given set of phase-shifts $\mathbf{\Delta}$, solution of the other three unknowns follows the linear least-squares algorithm described previously, and the global error function is easily calculated. Starting with an initial *guess* for the values of $\mathbf{\Delta}$ (e.g. $\Delta_n = n\pi/2$), the individual phase-shifts may be given small increments so as to minimize E^2 globally.

Because Δ_n and ϕ appear together in the argument of the cosine in Eq. (25), there is ambiguity in the definition of a *zero reference* phase point. This indicates that there are infinite degenerate solutions available. By defining the first phase position as *zero*, $\Delta_0 \equiv 0$, and defining all other phase steps with respect to it, we can exploit this ambiguity and remove one degree of freedom from the calculation. Solution proceeds as a minimization of E^2 in an $(N-1)$-dimensional space.

Global minimization should produce the optimum set of fit parameters. Although the authors of this method claim successful minimization is easily accomplished, experience with the implementation of this algorithm using a wide variety of minimization algorithms has shown otherwise. Inherent in Eq. (27) is a *high-degree of interdependence* among the individual phase-shifts Δ_n, leading to instability in the solution algorithm. Changing one of the phase-shift parameters by a small amount requires that each of the others must also be adjusted to minimize the error function. Perhaps if the initial guess is very close to the minimizing solution, then the problem can be made linear in the variations of $\mathbf{\Delta}$. Such considerations are beyond the scope of this thesis. Otherwise, a superior method must be found.

12.4.2 *The Fourier-Transform Method of Phase-Shift Determination*

With all other experimental conditions held fixed, the relative phase increments generated in phase-shifting interferometry are easily and accurately discernible in the Fourier-domain in the presence of a spatial-carrier-frequency. This section describes a novel yet very simple method of utilizing the spatial-frequency-domain information to discover the individual relative phase-increments from a phase-shifting series of interferograms. The application of this method and a comparison to other phase-shifting methods of analysis are presented in Section 8.10.2.

Many interferometric techniques, including the PS/PDI, require the introduction of a spatial-carrier-frequency, that is, *tilt fringes*. The PS/PDI acquires tilt as a by-product of the required beam-separation in the image-plane. In addition, *all* of the single-interferogram analysis methods discussed in Chapter 11 require the introduction of a significant amount of tilt. For successful analysis, the Fourier-transform

methods of single interferogram analysis require the presence of a spatial-carrier-frequency to adequately separate and isolate one of the information-carrying side-lobes.

As before, the expression for the *n*-th interferogram in a series may be written as

$$I_n(\mathbf{r}) = A(\mathbf{r}) + B(\mathbf{r})\cos[\phi(\mathbf{r}) + \Delta_n] = A(\mathbf{r}) + B(\mathbf{r})\cos[\phi(\mathbf{r}) + \mathbf{k}_o \cdot \mathbf{r} + \Delta_n],\tag{28a}$$

where
$$\phi(\mathbf{r}) \equiv \phi_o(\mathbf{r}) + \mathbf{k}_o \cdot \mathbf{r}.\tag{28b}$$

Here, following the discussion of Section 11.3, the general expression of the wavefront phase is represented by three separate terms: the *piston* term Δ_n contains all constant offsets; all *tilt* components, including the spatial-carrier-frequency, are collected in $\mathbf{k}_o \cdot \mathbf{r}$; $\phi_o(\mathbf{r})$ is comprised of all of the higher-ordered aberrations that are of interest to the interferometric measurements. By this definition, the piston and tilt components of $\phi_o(\mathbf{r})$ are identically zero.

Neglecting for the moment the presence of the discretely sampled domain, the Fourier-transform of $I_n(\mathbf{r})$ will be simplified by expansion of the cosine term:

$$I_n(\mathbf{r}) = A(\mathbf{r}) + B(\mathbf{r})\cos[\phi_o(\mathbf{r}) + \mathbf{k}_o \cdot \mathbf{r} + \Delta_n] = A(\mathbf{r}) + \tfrac{1}{2}B(\mathbf{r})e^{i[\phi_o(\mathbf{r}) + \mathbf{k}_o \cdot \mathbf{r} + \Delta_n]} + \tfrac{1}{2}B(\mathbf{r})e^{-i[\phi_o(\mathbf{r}) + \mathbf{k}_o \cdot \mathbf{r} + \Delta_n]}.\tag{29}$$

$$I_n(\mathbf{r}) = A(\mathbf{r}) + e^{i\Delta_n}C(\mathbf{r})e^{i\mathbf{k}_o \cdot \mathbf{r}} + e^{-i\Delta_n}C^*(\mathbf{r})e^{-i\mathbf{k}_o \cdot \mathbf{r}},\tag{30}$$

where
$$C(\mathbf{r}) \equiv \tfrac{1}{2}B(\mathbf{r})e^{i\phi_o(\mathbf{r})}.\tag{31}$$

and * indicates the complex conjugate.

The Fourier-transform of $I_n(\mathbf{r})$ is $i_n(\mathbf{k})$, given by

$$F\{I_n(\mathbf{r})\} = i_n(\mathbf{k}) = a(\mathbf{k}) + e^{i\Delta_n}c(\mathbf{k} - \mathbf{k}_o) + e^{-i\Delta_n}c^*(\mathbf{k} + \mathbf{k}_o).\tag{32}$$

By the same assumptions made in Section 11.3 regarding the spatial-frequency content of $A(\mathbf{r})$, $B(\mathbf{r})$ and $\phi(\mathbf{r})$, $a(\mathbf{k})$ and $c(\mathbf{k})$ both peak about the zero-frequency. Furthermore, although $a(\mathbf{k})$ may contain high-frequency and low-frequency components, it is assumed to be *quiet* in the vicinity of $\mathbf{k}_o$. The presence of the spatial-carrier-frequency displaces c and c^* and creates a Hermitian distribution with a zero-frequency peak and two side-lobes centered about $\mathbf{k}_o$ and $-\mathbf{k}_o$ respectively.

At the carrier-frequency

$$i_n(\mathbf{k}_o) = a(\mathbf{k}_o) + e^{i\Delta_n}c(0) + e^{-i\Delta_n}c^*(2\mathbf{k}_o).\tag{33}$$

$i_n(\mathbf{k}_o)$ is dominated by one of the side-lobes, and may be written as

$$i_n(\mathbf{k}_o) \approx e^{i\Delta_n}c(0).\tag{34}$$

Equation (33) enables us to access the individual *global* phase-steps Δ_n to within an arbitrary and unimportant offset angle.

$$\Delta_n \approx \tan^{-1}\left[i_n(\mathbf{k}_o)\right], \ \text{ or } \ \Delta_n \approx \text{Im}\left\{\ln\left[i_n(\mathbf{k}_o)\right]\right\}. \tag{35}$$

At this point, the individual phase-steps can be calculated and applied to the phase recovery as described previously. The additional additive phase angle determined by the complex constant $c(0)$ may be absorbed into the piston term in the analysis. Calculation of the individual phase-steps requires only that the Fourier-transform be calculated at one point, the carrier-frequency.

The following two sections introduce a method of carrier-frequency determination and assess the quality of the approximation made in Eqns. (34) and (35) and the effect of the discrete domain.

12.4.2.1 *Carrier-Frequency Determination*

The Fourier-transform method of phase-shift determination requires knowledge of the carrier-frequency $\mathbf{k}_o$. Experimentally, there are several ways of various complexity to determine $\mathbf{k}_o$ from the data. To implement these procedures, no wavefront aberration information is needed, and the entire interferogram is not required. If fact, these methods work best when only a sub-domain of the interferogram with complete fringe-coverage is used.

The most direct carrier-frequency determination method finds $\mathbf{k}_o$ approximately by locating the side-lobe peak in the spatial-frequency domain. In fact this required step is performed in the Fourier-transform method of single interferogram analysis (Section 11.3). When the side-lobe peak is located within the discrete Fourier-transform (DFT) spectrum, the uncertainty due to the discretization is one-half of the discretization size — typically, this is 0.5 cycles. This uncertainty can be reduced to any arbitrary size by increasing the resolution of the discrete spatial-frequency domain in the calculation.

A second two-step method uses the measured wavefront slope to determine the carrier-frequency. First, the Fourier-transform method of single-interferogram analysis is applied to a single interferogram in the series and a modulo 2π wavefront phasemap is generated. Heavy spatial-filtering can be used to simplify this procedure. After the phasemap is unwrapped, polynomial fitting procedures can be used to determine the components of *tilt* in the *x*- and *y*-directions. Let $\mathbf{t}$ be the tilt vector defined as

$$\mathbf{t} \equiv (x\text{-tilt}, \ y\text{-tilt}). \tag{36}$$

Here, the *magnitude* of $\mathbf{t}$ is defined as half of the peak-to-valley amplitude of the wavefront phase it describes. In this case, $\mathbf{k}_o$ is easily found.

$$\mathbf{k}_o = 2\mathbf{t}. \tag{37}$$

However $\mathbf{k}_o$ is calculated, there may be some uncertainty. Assume that while $\mathbf{k}_o$ is the *true* carrier-frequency, attempts to calculate $\mathbf{k}_o$ yield the value $\mathbf{k}'$ where

$$\mathbf{k}' \equiv \mathbf{k}_o + \boldsymbol{\varepsilon}. \tag{38}$$

$\boldsymbol{\varepsilon}$ is a vector in the spatial-frequency domain of magnitude much less than $\mathbf{k}_o$. The dependence of the

phase determination on $\boldsymbol{\varepsilon}$ can be seen from Eq. (33), with $\mathbf{k}'$ replacing $\mathbf{k}_o$:

$$i_n(\mathbf{k}') = i_n(\mathbf{k}_o + \boldsymbol{\varepsilon}) = a(k_o + \boldsymbol{\varepsilon}) + e^{i\Delta_n} c(\boldsymbol{\varepsilon}) + e^{-i\Delta_n} c^*(2\mathbf{k}_o + \boldsymbol{\varepsilon})$$

$$\approx e^{i\Delta_n} c(\boldsymbol{\varepsilon}) \tag{39}$$

The approximations of Eqns. (34) and (35) are still valid, but with a different leading constant. Depending on $\boldsymbol{\varepsilon}$, the magnitude of $c(\boldsymbol{\varepsilon})$ may be less than $c(0)$. The implications of this are discussed in the following section.

12.4.2.2 *Error Estimation*

The accuracy of phase-shift determination using the spatial-frequency-domain depends on the relative amplitudes of the functions $c(\mathbf{k}-\mathbf{k}_o)$, $c^*(\mathbf{k}+\mathbf{k}_o)$, and $a(\mathbf{k})$, near $\mathbf{k} = \mathbf{k}_o$. The phase of interest Δ_n is found in the coefficient of $c(\mathbf{k}-\mathbf{k}_o)$ in Eq. (33) and is given approximately by Eq. (35). The error in this approximation cannot be determined while $c(\mathbf{k})$ and $a(\mathbf{k})$ are unknown. However, by examining the data in a phase-shifting series an estimate of the error magnitude is easily made.

For an individual phase-step, the three quantities $c(\mathbf{k}-\mathbf{k}_o)$, $c^*(\mathbf{k}+\mathbf{k}_o)$, and $a(\mathbf{k})$ plus the Δ_n-dependent complex coefficients found in Eq. (33) may be regarded as complex scalars, or vectors in the complex plane. Assuming that all other experimental conditions are held fixed while the phase-shifting is implemented, only the unit-magnitude coefficients of $c(\mathbf{k}-\mathbf{k}_o)$ and $c^*(\mathbf{k}+\mathbf{k}_o)$ are affected. To separate the one term of interest from the other two, define two complex constants p and q.

$$p \equiv e^{i\Delta_n} c(0)$$

$$q \equiv a(\mathbf{k}_o) + e^{-i\Delta_n} c^*(2\mathbf{k}_o) \tag{40a, b, c}$$

$$i_n(\mathbf{k}_o) = p + q$$

p represents the phase of the side-lobe peak. q is the magnitude of the additional components. In most experimental situations of interest, it is safe to assume that $p \gg q$ and that the phases of p and q are independent.

Figure 2 shows a representation of p for six 60°-phase-steps in the complex plane. Only the resultant vectors are measurable. The largest phase error (between p and the measured value of $i(\mathbf{k}_o)$) occurs when q is perpendicular to p. When q is significantly smaller than p, the maximum magnitude of the error in the measured phase $\delta\Delta_n$ is approximately

$$\delta\Delta_n \lesssim |p|/|q| . \tag{41}$$

Since the $\delta\Delta_n$ depends on the ratio of $|q|$ to $|p|$, minimization of the error can occur in two ways. $|p|$ is increased by ensuring that the calculated carrier-frequency occurs at the peak value of the spatial-frequency domain side-lobe $c(\mathbf{k}-\mathbf{k}_o)$. $|q|$ depends on the mid-spatial-frequency content of $c^*(\mathbf{k})$ and $a(\mathbf{k})$, and can

only be minimized by guaranteeing that the spatial-carrier-frequency in use is of sufficient magnitude for this to be true. Improvements in fringe contrast reduce the relative magnitude of $a(\mathbf{k})$ and improve the ratio.

Although the magnitude of q is unknown, it may be estimated from the data. The variation in the measured magnitude of $i_n(\mathbf{k}_o)$ is related to the magnitude of q. This variation is represented by the gray ring in Fig. 2. The outer and inner radii of the ring are determined by $\max\{|p-q|\}$ and $\min\{|p-q|\}$, respectively. $i_n(\mathbf{k}_o)$ is maximum when p and q have the same phase, and minimum when p and q are 180° out of phase. The limitation of this estimation is that for a small sampling of phase-shift steps, there is no guarantee that the maximum and minimum values of $i_n(\mathbf{k}_o)$ will be achieved.

$$|q| \gtrsim \tfrac{1}{2}\left[\max\{|i_n(\mathbf{k}_o)|\} - \min\{|i_n(\mathbf{k}_o)|\}\right]. \tag{42}$$

Combining Eqns. (41) and (42), based on the measured data the estimated uncertainty in any given phase-step is

$\longrightarrow$: $e^{i\Delta_n}c(0)$

$\uparrow$: $a(\mathbf{k}_o) + e^{-i\Delta_n}c*(2\mathbf{k}_o)$

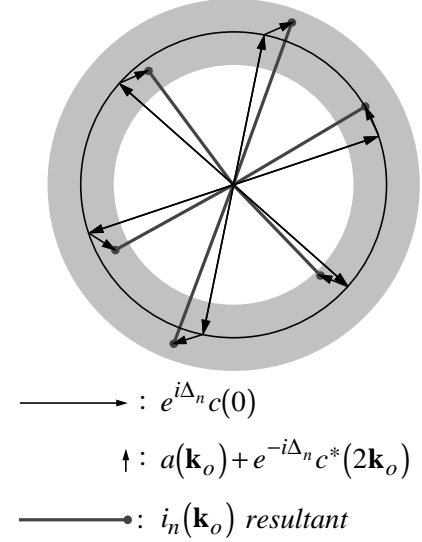$\longrightarrow\!\bullet$: $i_n(\mathbf{k}_o)$ *resultant*

Figure 2. A complex-plane representation of the side-lobe peak p, for six phase-shifting steps of 60°. The measured phase at the carrier frequency $i(\mathbf{k}_o)$ is dominated by p, but is affected by the non-zero magnitude of the other spatial-frequency-domain components q. q causes errors in the phase-determination. The gray ring shows that the maximum and minimum measured values of $i(\mathbf{k}_o)$ can be used to estimate q.

$$\delta\Delta_n \gtrsim \frac{1}{2|p|}\left[\max\{|i_n(\mathbf{k}_o)|\} - \min\{|i_n(\mathbf{k}_o)|\}\right] \approx \frac{\left[\max\{|i_n(\mathbf{k}_o)|\} - \min\{|i_n(\mathbf{k}_o)|\}\right]}{2|i_n(\mathbf{k}_o)|} . \tag{43}$$

13

Phase Unwrapping

13.1 INTRODUCTION

Due to the periodic nature of interference fringes, and the absence of an absolute reference point in phase, nearly all modern interferogram analysis phase-recovery methods are only capable of determining the wavefront phase to within an arbitrary multiple of 2π (occasionally, only to within a multiple of π). This limitation does not, however, restrict measurement to optical path differences (OPDs) of less than half of a wavelength: usually, there is sufficient information to reconstruct the original continuous wavefront from the available discontinuous data.

This chapter describes several approaches for solving this important inverse problem, and presents two novel methods. One method is designed to overcome the difficulties presented by numerous, isolated regions containing no valid data. A second, very general and robust method is capable of operating in low signal-to-noise applications and, where valid data exists, in isolated, discontiguous regions.

13.1.1 *Unwrapping Overview*

For reasons addressed in Chapter 12, many phase-retrieval methods combine several separate interference patterns and utilize a relation based on an arctangent to recover the wavefront phase. Other methods, based on Fourier-domain analysis, also utilize an arctangent.

In general, the calculated phase $\phi'(\mathbf{r})$ may be written as a functional, combining N separately measured interferograms $\{I_1, \ldots, I_N\}$:

$$\phi'(\mathbf{r}) = \tan^{-1}\left\{F\left[I_1(\mathbf{r}), I_2(\mathbf{r}), \cdots, I_N(\mathbf{r})\right]\right\} . \tag{1}$$

Each point in $\phi'(\mathbf{r})$ is related to the actual wavefront $\phi(\mathbf{r})$ by an arbitrary number of 2π steps. $\phi'(\mathbf{r})$ is called a *modulo 2π phasemap* and is related to the actual wavefront phase by the relation

$$\phi'(\mathbf{r}) = \phi(\mathbf{r}) \bmod 2\pi . \tag{2}$$

Here the modulus function is defined as the remainder after the largest integer multiple of 2π less than or equal to $\phi(\mathbf{r})$ has been subtracted. Figure 1 illustrates this point in one dimension, showing both the original wavefront and the modulo 2π measured wavefront.

Equation (2) forms the basis of one of the most important and often extremely difficult inverse problems in modern interferogram analysis: the modulo 2π phasemap must be used to reconstruct the
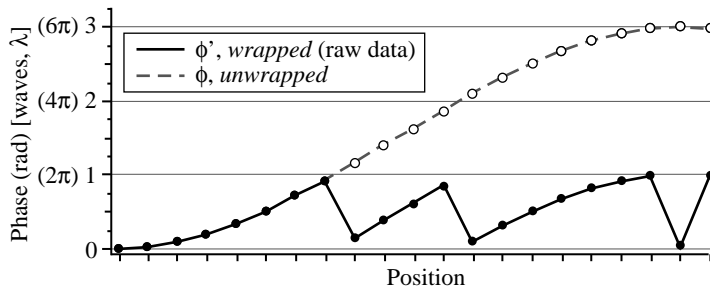

Figure 1. Although the test wavefront is continuous (dashed line), the raw phase data from interferogram analysis is typically modulo 2π, or modulo λ. The goal of *phase unwrapping* is to reconstruct the original continuous wavefront from the raw data.
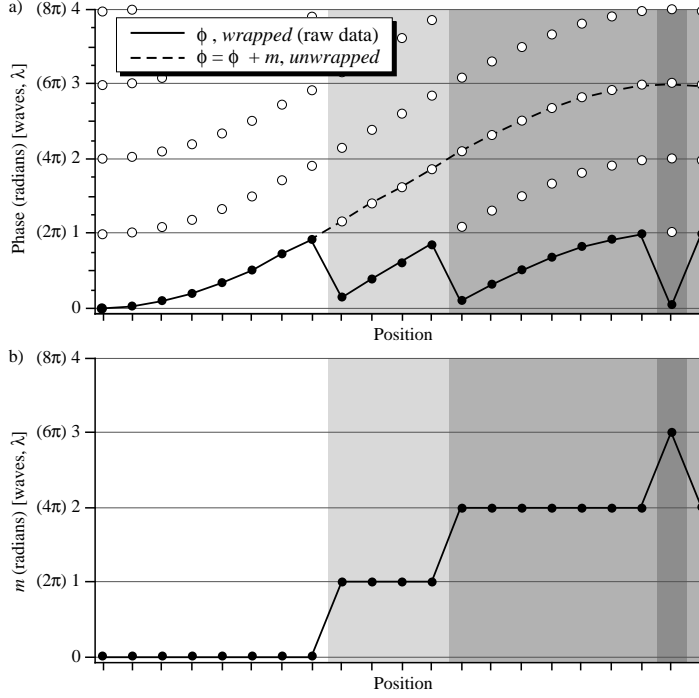
Figure 2. Reconstruction of the test wavefront from the wrapped raw data requires that each point be incremented by an integral number of wavelengths (2π radians), to achieve a surface free of discontinuities. (a) Based on the raw data (black circles) the hollow circles represent the available choices for each point in the reconstruction. (b) The calculated increments are stored in the array m.

actual wavefront, such that $\phi(\mathbf{r})$ is the surface of least curvature, with its 2π discontinuities removed by the reconstruction.

While an obvious approach may simply require the addition of 2π steps wherever a discontinuity is detected, the problem becomes complicated in the presence of noise, or where the data exists in disjoint regions. Another source of difficulty arises when the spatial-frequency of the fringes approaches the Nyquist limit (Nyquist 1928), and the local wavefront slope exceeds individual steps of π *continuously*. Such extreme cases, not discussed here, may require *a priori* information and utilize the so-called Sub-Nyquist Interferometry (SNI) methods developed by Grievenkamp (1987).

In each method presented here, the goal is to determine empirically the function $m(\mathbf{r})$ that solves

$$\phi(\mathbf{r}) = \phi'(\mathbf{r}) + m(\mathbf{r}), \text{ where } m(\mathbf{r}) = 2\pi n(\mathbf{r}), \ n \in \textit{Integers} . \tag{3}$$

Fig. 2 shows the role of $m(\mathbf{r})$.

13.1.2 *Notation*

A change of units simplifies our notation considerably. Using *wavelength* units rather than *radians* to describe the wavefront phase $\phi(\mathbf{r})$ and $\phi'(\mathbf{r})$ enables $m(\mathbf{r})$ to take integer values. For this notation, Eqns. (2) and (3) must be re-written as

$$\phi'(\mathbf{r}) = \phi(\mathbf{r}) \bmod 1 , \tag{4}$$

and

$$\phi(\mathbf{r}) = \phi'(\mathbf{r}) + m(\mathbf{r}), \ m(\mathbf{r}) \in \textit{Integers} . \tag{5}$$

The modulo 1 function retains only the fractional part of $\phi(\mathbf{r})$, between 0 and 1, *including* zero. Here, $\phi'(\mathbf{r})$ is referred to as the *modulo λ phasemap*.

213

13.2 SIMPLE UNWRAP METHODS

Under favorable circumstances, procedures for unwrapping *modulo 2π phasemaps* (or *modulo λ phasemaps*, in wavelength units) are often very straightforward, iterative techniques. Complicated versatile and robust algorithms are often built on the careful application of the simple techniques. This section presents several general unwrapping methods of increasing complexity and usefulness. First, a one-dimensional treatment is presented and then is expanded to two dimensions. Next, the problem is generalized to withstand the presence of noise and to include arbitrary "continuous" aperture shapes. The specific continuity requirements are carefully described for each method.

As discussed in Section 13.1.1, the goal of phase unwrapping is to find the function $m(\mathbf{r})$, which is used to reconstruct the smooth phasemap $\phi(\mathbf{r})$ from the (potentially) discontinuous modulo λ phasemap $\phi'(\mathbf{r})$. From the previous section, the function is defined in the following way, in wavelength units:

$$\phi(\mathbf{r}) = \phi'(\mathbf{r}) + m(\mathbf{r}), \ m(\mathbf{r}) \in Integers. \tag{6}$$

One assumption of the following discussions is that we have no *a priori* knowledge of the uncertainty of any individual data point relative to the others. Some phase-unwrapping methods utilize varied data-validation techniques (Huntley 1989, Quiroga and Bernabeu 1994, Stephenson 1994, Charette and Hunter 1996) to eliminate spurious points or regions from further calculations. Here the assumption will be that *bad* points coexists with the rest of the data.

13.2.1 One-Dimensional Unwrapping

In principle, the discontinuities in $\phi'(x)$ are limited to a finite number of points. Excluding these points, $\phi'(x)$ and $\phi(x)$ are related by a (piecewise continuous) constant offset, and thus have the same derivative. Numerically, the discontinuities in $\phi'(x)$ are easily detected by examining the behavior of the discrete derivative of $\phi'(x)$, defined as

$$\frac{d\phi'}{dx} \equiv \frac{\phi'(x+1) - \phi'(x)}{1} = \phi'(x+1) - \phi'(x), \text{ where } x = 0, \ 1, \ 2, \ \cdots \tag{7}$$

For the purposes of this discussion, the term *derivative* refers to this discrete approximation. Discontinuities are present wherever the magnitude of the derivative exceeds a given threshold.
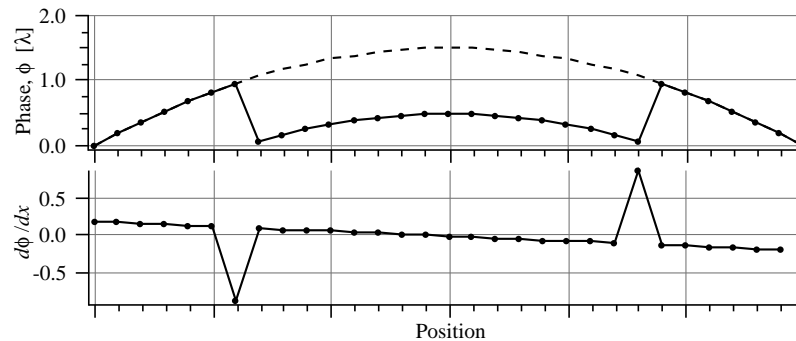

Figure 3. Modulo λ raw phase data ϕ' and the discrete derivative $d\phi'/dx$ as defined in Eq. (7) are shown to illustrate the use of the derivative in locating the phase discontinuities. Where the magnitude of the derivative exceeds a threshold value (e.g. 0.5 waves), a discontinuity is detected. The sign of the derivative is also used in the reconstruction.

214

Figure 3 shows the behavior of $\phi(x)$, $\phi'(x)$, and $d\phi'/dx$, where $d\phi'/dx$ is defined on the discrete domain, with x as the index of the point. Where the magnitude of the derivative exceeds 0.5 (waves), a discontinuity is present. The sign of the derivative reveals whether the step is up or down.

To construct $m(x)$ from $\phi'(x)$ and $d\phi'/dx$, one may scan across the domain of N points and increment $m(x)$ according to the following procedure.

Procedure 1: Basic One-Dimensional Unwrap
1. Loop i from 1 to $(N-1)$
2. $\quad$ $\Delta_x = \phi'(i + 1) - \phi'(i)$ $\qquad\qquad\qquad$ (*horizontal discrete derivative*)
3. $\quad$ IF $|\Delta_x| > 0.5$ THEN
4. $\qquad$ $m(i + 1 \text{ to } N) \leftarrow m(i + 1 \text{ to } N) - \text{sign}(\Delta_x)$ $\quad$ (*shift all points from $i + 1$ to end of row*)

The sign function is defined as

$$sign(x) \equiv \begin{cases} -1, & x < 0 \\ 0, & x = 0 \\ +1, & x > 0 \end{cases} . \tag{8}$$

The arrow operation "$\leftarrow$" indicates: *replace the quantity on the left with the quantity on the right*. (This operation is straightforward to perform on a computer.) In Step 4, all of the points in $m(x)$ that *follow* a discontinuity are affected. The use of the sign function, defined in Eq. (8), implements an increasing *or decreasing* step where appropriate.

The *threshold value* on the magnitude of the derivative (here defined as 0.5 in Step 3) determines the maximum allowable wavefront slope for proper reconstruction. Any slope greater than this value is identified as a discontinuity where the phase is wrapped.

Application Note. In experimental applications, one fact about this unwrap method is abundantly clear: Procedure 1 is very vulnerable to bad data. A single "error" can create an erroneous offset in all of the subsequent data. It is possible to incorporate several neighboring points into the derivative calculation in order to overcome the effects of a single spurious data point. In such cases, care must be taken to properly handle discontinuities when they occur at the edges of a domain. Methods of this sort can also be effective where the wavefront slope is large.

Another approach is to pre-filter the data before unwrapping, either in one- or two-dimensions. Simple *smoothing* or *averaging* filters should be avoided because they improperly smooth the necessarily sharp 2π phase-discontinuities and may reduce their magnitude below the threshold required for detection. Furthermore, smoothing causes a loss of high-frequency information that may be of interest. In the presence of an isolated bad point, a *smoothing* filter will decrease the magnitude of the difference by distributing the magnitude among a neighborhood of adjacent points.

Some authors have recommended the median filter (Freiden 1981, Crennell 1993) as one capable

of reducing isolated *bad points* while preserving the sharpness of the phase discontinuities. Since a median filter samples a small neighborhood of points and replaces the value at the center with the median value of the group, it can bring an isolated bad point into agreement with its neighbors without affecting adjacent points. This is a very important advantage of the median filter.

13.2.2 *Two-Dimensional Unwrapping*

Two-dimensional unwrapping is required for most interferogram wavefront analysis. It may be considered as the direct extension of one-dimensional unwrapping to rows *and* columns of data. First, the *x*-direction derivative is used to implement the horizontal row unwrapping of Procedure 1. In the absence of noise, this ensures the continuity of ϕ in the *x*-direction only. A second step then utilizes the *y*-direction derivative to increment entire rows. During the procedure, it may occur that the magnitudes of some discontinuities become larger than 1.5. In these cases, the required increments (or decrements) of *m* become greater than 1. Any row-incrementing routine must address this issue either by using multiple unwrapping "passes" through the data or by sensing the magnitude of each required increment.

Note that for the purpose of phase unwrapping on a two-dimensional data set, the *x*-direction is chosen arbitrarily. Clearly, when the orientation of the unwrapping procedure is rotated by 90°, the resultant phasemap must be the same to within a constant multiple of λ. Separately unwrapping in two orientations can be used as a method of data validation. A comparison can be used to quickly identify problematic regions.

The most basic procedure for two-dimensional unwrapping is outlined below. As a simplified notation, an asterisk used as an index represents an entire row or column of the domain. For instance, $\phi'(*,2)$ is the entire second row, and $\phi'(3,*)$ is the third column.

Procedure 2: Basic Two-Dimensional Unwrap	
1. Loop *j* from 1 to *N*	
2. Implement Procedure 1: on each row $\phi'(*, j)$	*(1-D unwrap)*
3. Choose a single column, $x = x_o$, to use as a *guide* for vertical unwrapping	
4. Loop *j* from 2 to *N*	
5. $\Delta_y = \phi'(x_o, j) - \phi'(x_o, j-1)$	*(vertical derivative)*
6. IF $|\Delta_y| > 0.5$ THEN	
7. $m(*, j) \leftarrow m(*, j) - \text{sign}(\Delta_y) * \text{floor}(|\Delta_y|)$	*(shift row)*

The function floor(*x*) is defined as the greatest integer less than or equal to *x*.

The most significant limitation of Procedure 2 is that just one column is arbitrarily chosen as a guide for the vertical unwrapping. As with the one-dimensional unwrapping of Procedure 1, a single bad data point in this particular column affects the subsequent unwrapping of all of the rows.

Experience has shown that simple methods of filtering the derivative can substantially improve unwrapping results in the presence of noise. If the row increment is based instead on the *average vertical*

derivative across the width of the array, then many more points are considered, reducing the effects of a single bad data point. However, it is quite possible for one or several points very far in magnitude from the neighboring values to strongly influence the average derivative.

A superior filter is the median. When the *median vertical derivative* is used, a large number of *bad* data points, or several points that are far from their neighboring values, will not affect the calculated derivative. In this way, the effects of bad data points do not propagate as easily into other rows.

A method for incorporating the median in the vertical unwrap is given in Procedure 3.

Procedure 3: Two-Dimensional Unwrap with a Median Filter		
1.	Loop j from 1 to N	
2.	Implement Procedure 1: on each row $\phi'(*, j)$	(*1-D unwrap*)
3.	Loop j from 2 to N	
4.	$\Delta_y \equiv \text{median}\{\phi'(*, j) - \phi'(*, j - 1)\}$	(*median difference*)
5.	IF $\left|\Delta_y\right| > 0.5$ THEN	
6.	$m(*, j) \leftarrow m(*, j) - \text{sign}(\Delta_y) * \text{floor}\left(\left|\Delta_y\right|\right)$	(*shift row*)

13.2.3 *Unwrapping on Sub-Domains*

Interferogram fringe patterns are often collected on a sub-region of a detector array. Consequently, the relevant regions containing phase information are sub-regions of a larger available domain. A broad class of versatile phase unwrapping algorithms accommodates the arbitrary positions and shapes of these domains, and avoids the inclusion of points from outside of the valid sub-region.

In this section two methods are presented for addressing sub-domain unwrapping. The first method places strict requirements on the shape of the sub-region and is therefore limited in its applicability. The second, more general method extends the capabilities of the first to a wider variety of sub-region shapes.

For the purposes of this discussion, the selection of the sub-domain of interest must be done prior to the unwrapping calculation. This may be done in a number of ways: manual methods, involving user-interactive procedures, or automatic methods, in which an investigation of signal-to-noise or some other relevant property helps to identify the sub-regions of valid data. As mentioned previously, some calculation-intensive methods are capable of validating data *during* the analysis. It is not be necessary to address those methods here.

We can describe sub-regions of interest with the definition of a special binary function $o(\mathbf{r})$ across the full domain of measurement. $o(\mathbf{r})$ is used throughout this discussion.

$$o(\mathbf{r}) \equiv \begin{cases} 1, & \forall\, \mathbf{r} \in \text{sub - region} \\ 0, & \forall\, \mathbf{r} \notin \text{sub - region} \end{cases}. \tag{9}$$

Sub-Domain Unwrapping: Method 1

This method places two requirements on the shape of the sub-region.
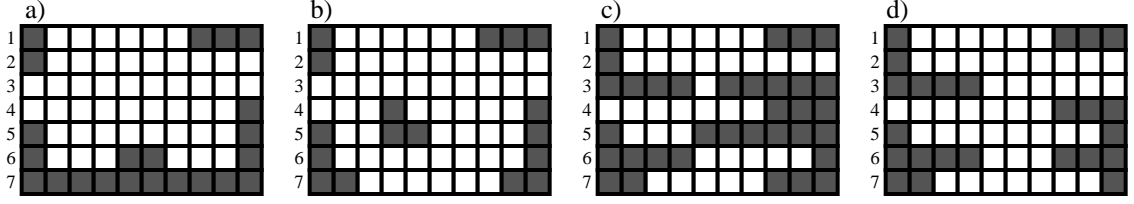
217

Figure 4. This figure illustrates the requirements on the sub-domain unwrapping imposed by Procedure 4 of Method 1. White squares belong to the sub-domain of interest. Row 6 of (a) is discontinuous. Likewise, rows 4 and 5 are discontinuous in (b). All of the rows of (c) are continuous, yet vertical connectedness is violated by rows 5 and 6, which share no common columns. (d) satisfies both of the requirements and is a valid sub-domain for unwrapping by Method 1.

> 1. **Row Continuity**: The horizontal path between any two points in the same row within the sub-domain must not include any points outside the domain. That is, the horizontal rows of the sub-region must not be discontinuous.
> 2. **Vertical Connectedness**: Any two adjacent rows within the sub-domain must contain at least one column in common.

Figure 4 illustrates these requirements.

Procedure 4 is a modification of the median-filtered two-dimensional unwrapping Procedure 3, refined to include only points within the sub-domain defined by $o(\mathbf{r})$.

Procedure 4: Two-Dimensional Median-filtered Unwrap on a Sub-Domain	
1. Loop j from 1 to N	
2. Implement Procedure 1, on each row $\phi'(*, j)$	(*1-D unwrap*)
3. Loop j from 2 to N	
4. $i^* \equiv \{i \mid o(i, j) = 1 \text{ AND } o(i, j - 1) = 1\}$	(*vertical connectedness*)
5. IF $i^* \neq \varnothing$ THEN	(*note: $\varnothing$ denotes the* empty set)
6. $\Delta_y \equiv \text{median}\{\phi'(i^*, j) - \phi'(i^*, j - 1)\}$	(*median difference*)
7. IF $|\Delta_y| > 0.5$ THEN	
8. $m(*, j) \leftarrow m(*, j) - \text{sign}(\Delta_y) * \text{floor}(|\Delta_y|)$	(*shift row*)

The symbol $\varnothing$ denotes the *empty set*.

It is not necessary, to restrict the row-unwrapping of Step 2 to include only points within the sub-region, points outside of the sub-region will be ignored by the use of i^* in Step 6. Between every pair of adjacent rows, the median difference Δ_y calculated in Step 6 is based only on those pairs of points that share a column. This is illustrated in Fig. 5. The arrows indicate which pair of rows is being compared. In the figure, the elements that would be used in the calculation of Δ_y are marked with an "X". Note that if a row contains no valid points of the sub-region, no calculation is performed. By the two requirements above, it is clear that this only occurs at the bottom row and at the first empty row above the sub-region.

By invoking median filtering in Step 6, Procedure 4 is more resistant to noise than Procedure 3.
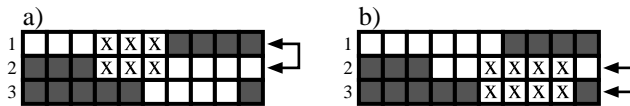

Figure 5. In Procedure 4, Step 6, the median difference between two rows (a vertical derivative) is calculated using only points from columns common to both rows. Here the arrows indicate which two rows are being compared, and the "X" symbols mark the specific points that are used.
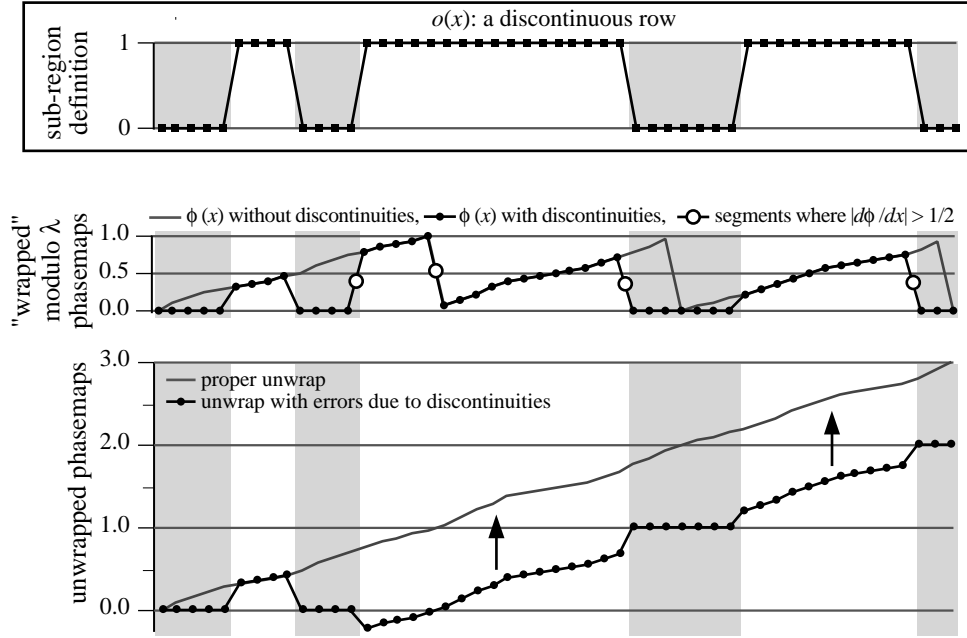
Figure 6. Row unwrapping in the presence of discontinuities can lead to unwrapping errors. The domain is defined by the binary function $o(x)$, shown in the top plot. $o(x) = 1$ for points within the domain. The middle plot shows a modulo λ raw phasemap (dots), set to zero within the discontinuities. The solid grey line shows what the raw phasemap would be if the obstructions were removed. The hollow circles indicate the places where magnitude of the derivative exceeds 0.5, triggering a phase increment in the unwrapping algorithm. The bottom plot compares the unsuccessfully unwrapped phasemap (dots) with the ideal case (grey line). Here, errors are caused by phase-wrapping occurring within the obstruction, *and* by the obstruction itself.

However, the application of Procedure 4 is limited to special kinds of sub-regions. For example, it is incapable of properly unwrapping in the presence of row discontinuities; Fig. 6 illustrates why. There are two kinds of errors that can be introduced when this procedure is followed in the presence of discontinuities. One type of error arises when a phase-wrap occurs *within* a discontinuity. The second type causes a phase-step to be assigned (correctly or erroneously) *because of* the discontinuity, wherever the magnitude of the derivative exceeds 0.5 (waves); these points are indicated in the figure by hollow circles.

It is possible to improve Procedure 4 to identify and correctly account for horizontal discontinuities. Therefore, sub-regions containing "holes" can be properly unwrapped. This method is outlined in Procedure 5.

The less-restrictive sub-region requirements for Procedure 5 are as follows.

1. **Row Continuity** is required only of the *first row*. The horizontal path between any two points in first row of the sub-domain must not include any points outside of the sub-domain. That is, the first row of the sub-region must be continuous.
2. **Vertical Connectedness:** Any two adjacent rows within the sub-domain must contain at least one column in common. Further, if a row *is* discontinuous, then each separate, continuous part of the row must be vertically connected to the *previous* row by at least one point within the sub-domain.

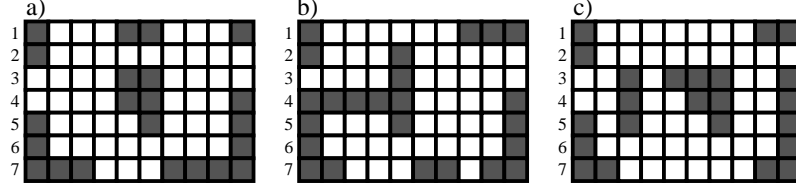These two requirements are illustrated in Figure 7.

Figure 7. These three figures illustrate the requirements imposed on the sub-domain shape by Procedure 5. Row 1 of (a) is discontinuous and so violates the first requirement. (b) The segment on the left side of row 5 is not vertically connected with the rows above it. (c) Both requirements are satisfied. This illustrates how this method can successfully address surrounded obstructions in the centers of sub-domains.

Procedure 5 Two-dimensional Median-filtered Unwrap on a General Sub-Domain

1.   Loop j from 1 to N
2.   Implement Procedure 1, on each row $\phi'(*, j)$ (*1-D unwrap*)
3.   Loop j from 2 to N
4. $c \equiv$ number of separate, continuous regions in row $\phi'(*, j)$
5.   Loop k from 1 to c
6. $i_k \equiv \{i \mid i \in$ the kth continuous region of $o(*, j) = 1 \}$
7. $i_k^* \equiv \{i_k \mid o(i_k, j) = 1 \text{ AND } o(i_k, j - 1) = 1\}$ (*vertical connectedness*)
8.   If $i_k^* \neq \varnothing$ then
9. $\Delta_y^k \equiv \text{median}\{\phi'(i_k^*, j) - \phi'(i_k^*, j - 1)\}$ (*median difference*)
10.   IF $\left|\Delta_y\right| > 0.5$ THEN
11. $m(i_k, j) \leftarrow m(i_k, j) - \text{sign}(\Delta_y^k) * \text{floor}\left(\left|\Delta_y^k\right|\right)$ (*shift row*)

There are a number of simple ways to count the separate continuous regions of a given row and identify their endpoints, as required by Steps 4 and 6. Besides scanning the individual pixels, the discrete derivative of the sub-region-defining function $o(x, y)$ can be used. Recalling that $o = 1$ for points within the sub-region and $o = 0$ for points outside of the sub-region,

$$\frac{do(x, y)}{dx} = o(x + 1, y) - o(x, y) = \begin{cases} 1, & \text{at the point } \textit{before} \text{ the start of a new continuous region} \\ -1, & \text{at the last point of a continuous region} \\ 0, & \text{at any other point} \end{cases} \quad . \quad (10)$$

Since this derivative is undefined at the edges of the domain, edge points must be considered separately. This problem is easily averted by padding the rows with a leading and a trailing zero.

Step 6 identifies the x-indices of points within the row's separate, continuous regions, one region at a time. It should be noted that these regions may be as small as one column wide. Step 7 then determines which of these points can be used in the calculation of the median difference Dyk. If |Dyk| exceeds 0.5 (waves), then all of the points within the particular continuous sub-region of the row are incremented by the appropriate integer to make the median difference less than 0.5 in wavelength units.

13.3 UNWRAPPING ISOLATED BAD REGIONS: PHASEMAP *CLEANING*

The unwrapping procedures presented in the previous sections have various amounts of resistance to noise in the raw phase data. By using filtered comparisons of adjacent rows, the more sophisticated

procedures attempt to stem the vertical propagation of errors. However, no attempt is made to limit horizontal error propagation within the rows. As a result, an imperfectly unwrapped phasemap may contain isolated points, horizontal lines, or whole regions of data that are *shifted* by an integral number of wavelengths away from a position that would provide the best agreement with adjacent data.

This very succinct procedure introduces a method that has been successfully used to *clean* unwrapping errors.

> **Procedure 6: Phasemap Cleaning**
> 1. Break the interferogram into N rectangular tiles: name the individual tile domains D_n.
> 2. Loop n from 1 to N
> 3. $m_n \equiv \text{median}[\phi(D_n)]$ (*tile median*)
> 4. $\Delta(D_n) \equiv \text{round}[\phi(D_n) - m_n]$ (*point-by-point comparison*)
> 5. $d \equiv \text{round}(m_n - m_{n-1})$ (*adjacent tile comparison*)
> 6. $\phi'(D_n) \equiv \phi(D_n) - \Delta(D_n) - d$ (*tile cleaning*)

First the interferogram is broken into individual tiles. Then each point in the domain is compared to the tile median with the round(x) function. By definition, round(x) returns the closest integer to x. The two-dimensional array $\Delta(D_n)$ is non-zero at any point that differs from the median by more than 0.5 waves. Similarly, this tile is compared to an adjacent *previously examined* tile (represented symbolically by the $n-1$ index), again using the round(x) function to calculate the scalar d. Finally, a new phase function ϕ' is calculated for the tile.

One significant aspect of this procedure is the use of the round(x) function rather than a comparative IF $\cdots$ THEN statement to identify the points that are more than 0.5 waves from the median. Rounding, which speeds-up and simplifies the procedure, is used again in Section 13.4 for Guided Unwrapping.

Refinements. There are several refinements of the basic method that can improve the results significantly. In the presence of high wavefront slope, or *tilt*, points at the edges of the tile may differ substantially from the median value. For this case, two possible solutions are as follows. First, choose a small tile size, or choose the length and width of the tile based on the mean wavefront slope in the x and y directions respectively — small tile for high slope. Another approach is to calculate and subtract the mean tilt within each tile, then calculate the median, repair the bad points, and, finally, replace the tilt that has been removed. This method makes the use of larger tile sizes possible.

Selecting the optimum tile size is a very difficult matter. Isolated points and lines are the easiest problems to repair. However, when a whole region is collectively shifted, a small tile may become engulfed. For example, the tile may fall completely within the shifted region, and the program may not recognize its displacement from the adjacent phase values. Therefore, the optimum tile size must not be smaller than any shifted regions. At the same time, if the wavefront curvature is large, the tile must not exceed the length-scale of wavefront variations under investigation. Otherwise, the curvature may impair

the proper calculation of the median. The comparison of the median values of adjacent tiles is intended to reduce the limitations of using small tiles. If a *cleaned* tile is compared to the previously-cleaned adjacent tile, then the cleaning process becomes analogous to the simple unwrapping process, performed on the tiles rather than on the individual pixels (i.e. the tiles become *super-pixels*).

Another improvement on these methods is to be aware of which points *within* a tile belong to the measurement domain and which points do not. Rectangular tiles will overlap irregular domain boundaries. The exclusion of points that fall outside of the domain may yield a median value more characteristic of the data within a tile.

A last approach is to perform the cleaning multiple times, using different tile sizes. Doing so, however, runs the risk of *introducing* unwrapping errors into a clean phasemap. To reduce the likelihood of this problem, two cleaning procedures can be performed *in parallel* and then compared for inconsistencies.

Special Note. At this point, the "cookbook" nature of these unwrapping "recipes" is certainly evident. Procedures and variations of procedures fill the literature, and there appears to be little agreement on which is the most reliable, most computationally efficient, and fastest method to use in arbitrary circumstances. The following sections on Guided Unwrapping seek to overcome these limitations by using an entirely different approach that has proved the most successful in EUV interferometry applications.

13.4 GUIDED UNWRAPPING

Unwrapping noisy data is perhaps the single most daunting task facing many interferogram analysis applications, and it was certainly a significant problem for the EUV interferometry experiments as described in this thesis. The unwrapping procedures presented in the previous sections utilize adaptable filtering methods to overcome some of the limiting effects of noise. These methods inevitably fall short of the mark and leave the unwrapped phasemaps with errors introduced by noisy data. Attempts to clean the unwrapped phasemaps improve the situation, but are not always reliable.

A completely different approach is the use of *a priori* wavefront information during the unwrapping procedure. Obviously, if the final result is already known, the unwrapping is trivial. However, when the wavefront is known only *approximately*, then the information contained in the approximate wavefront can be used to *guide* the unwrapping procedure with great success. In the guided unwrap, all of the high-frequency information in the raw data is preserved. Perhaps the most significant advantage of the guided unwrap is its ability to unwrap in the presence of obstructed regions and regions containing no valid data. Discontiguous sub-regions, for example, can be unwrapped without any special considerations. Unlike the previous unwrapping methods, guided unwrapping is equally applicable to any one- or two-dimensional domain because there is *no reliance* on neighboring data.

The concept of guided unwrapping is used in Sub-Nyquist Interferometry (Greivenkamp 1987) designed for cases in which the wavefront slope exceeds 0.5 waves per step (Nyquist limit), where conventional unwrapping methods fail. Here, a similar idea is exploited to overcome noise. How the *a priori* information is obtained is not important here. (Section 13.5 discusses a novel approach to ascertain the approximate wavefront required for guided unwrapping.)

The most simple guided unwrapping procedures are described in Procedures 1a and 1b below. Suppose that the *a priori* wavefront information is contained in the function $\Gamma(\mathbf{r})$ over the measurement domain. Using the raw phase data $\phi(\mathbf{r})$, the most simple guided unwrapping procedure utilizes the function $\text{round}(x)$ in a way that is similar to the phasemap cleaning procedures in Section 13.3 of this chapter.

Procedure 1a: Guided Unwrapping
1. $m(\mathbf{r}) \equiv \text{round}\big[\Gamma(\mathbf{r}) - \phi(\mathbf{r})\big]$ (*difference rounded to nearest integer*)
2. $\phi'(\mathbf{r}) \equiv \phi(\mathbf{r}) + m(\mathbf{r})$ (*adjust raw phasemap into agreement with the guide*)

More succinctly, this procedure may be written in one single step.

Procedure 1b: One-Step Guided Unwrapping
1. $\phi'(\mathbf{r}) \equiv \phi(\mathbf{r}) + \text{round}\big[\Gamma(\mathbf{r}) - \phi(\mathbf{r})\big]$

As in the unwrapping techniques presented in the previous sections, integer (wavelength) steps are added or subtracted from the raw data to produce the unwrapped phasemap. As before, the function $m(\mathbf{r})$ (Procedure 1a only) contains the required integer phase steps in wavelength units. Notice, however, that in
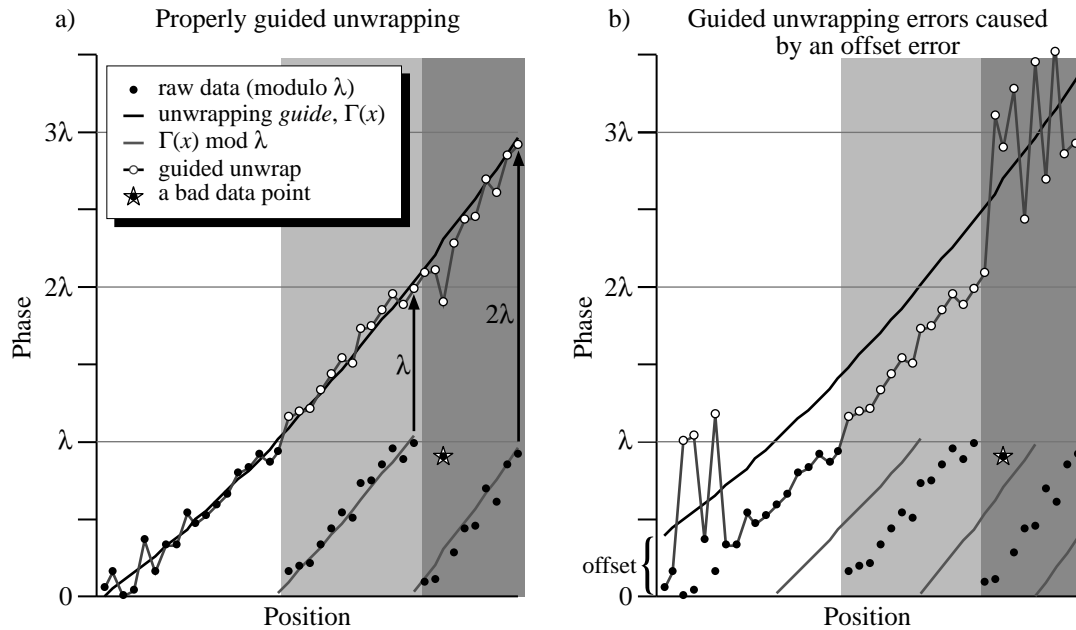
Figure 8. Guided unwrapping works successfully when the guide is approximately separated from the raw data by an integral number of wavelengths, as shown in (a). When there is a fractional offset, however, the proper increment for the raw data becomes ambiguous. In (b) the offset is approximately 0.5 waves. Small variations in the raw data cause the increment to fluctuate by one wave for adjacent points. This kind of guided unwrapping error is addressed by Procedures 2a and 2b.

contrast to the previous methods these procedures pay *no attention* to the locations of the discrete phase-wrapped steps present in the raw data. In fact it is not even necessary to differentiate between points that are inside or outside of the measurement domain: points outside of the domain are not included in subsequent analysis.

At this point, Procedures 1a and 1b contain one subtle oversight that can lead to unwrapping errors. Figure 8 illustrates two examples of the guided unwrapping procedures given in Procedures 1a and 1b above. Under ideal circumstances, shown in Fig. 8(a), the raw data $\phi(x)$ is brought into the best possible agreement with the unwrapping guide $\Gamma(x)$. Figure 8(b), however, illustrates a serious problem that occurs when there is a fractional *offset* between the raw data and the unwrap guide. In this case, there can be ambiguity in the unwrapping. Usually, individual data points are incremented to bring them as close to the guide as possible; but when the offset is close to 0.5 waves, small variations in the raw data can induce differences of one wave in the guided unwrap.

Procedures 2a and 2b, below, overcome the offset problem. The solution presented here is to compute the offset before the guided unwrap is performed. In the presence of noisy data this calculation requires some filtering, and the median filter again proves very useful. Here, it is very important to restrict **r** to points within the measurement domain D, this ensures that the median difference is a meaningful value (not based on invalid data from outside of the domain).

Procedure 2a: Guided Unwrapping with Offset Removal, Method 1
1. $\Delta \equiv \text{median}\left\{ [\Gamma(D) - \phi(D)] - \text{round}[\Gamma(D) - \phi(D)] \right\}$ (*calculate offset*)
2. $m(\mathbf{r}) \equiv \text{round}[\Gamma(\mathbf{r}) - \phi(\mathbf{r}) - \Delta]$ (*difference rounded to nearest integer*)
3. $\phi'(\mathbf{r}) \equiv \phi(\mathbf{r}) + m(\mathbf{r})$ (*adjust into agreement with guide*)

An equivalent yet slightly more succinct implementation of Step 1 above uses the *modulo* operation to perform the rounding and subtraction in one step. There is, however, one minor catch: the modulo operation becomes non-periodic at $x = 0$. Any problem this aspect of the modulo operation may cause may be avoided by ensuring that the difference between Γ and ϕ is positive-definite: a large number L may be added to Γ during the modulo operation.

Procedure 2b: Guided Unwrapping with Offset Removal, Method 2
1. $L \equiv any$ integer greater than $- \min\left\{ \Gamma(D) - \phi(D) \right\}$ (*e.g. choose 10,000*)
2. $\Delta \equiv \text{median}\left\{ [L + \Gamma(D) - \phi(D)] \bmod 1 \right\}$ (*calculate offset*)
3. $m(\mathbf{r}) \equiv \text{round}[\Gamma(\mathbf{r}) - \phi(\mathbf{r}) - \Delta]$ (*difference rounded to nearest integer*)
4. $\phi'(\mathbf{r}) \equiv \phi(\mathbf{r}) + m(\mathbf{r})$ (*adjust into agreement with guide*)

Both Procedures 2a and 2b may be simplified slightly by the combination of the last two steps into one single step, as was done in Procedure 1b.

13.5 FOURIER-TRANSFORM GUIDED UNWRAP

The guided unwrapping technique presented in Section 13.4 combines the desirable attributes of simplicity, speed, and high-reliability. The difficulty lies in obtaining the *a priori* approximation to the unwrapped wavefront being measured. This section presents a novel method of synthesizing the best attributes of two existing methods to produce a new unwrapping procedure called the *Fourier-Transform Guided Unwrap*.

In essence, the powerful spatial-filtering capability of the Fourier-transform technique is used to generate an *a priori* wavefront phasemap containing only low-spatial-frequency information. When used as an unwrapping guide for raw phase data generated by another means (e.g. phase-shifting), otherwise difficult unwrapping procedures are greatly simplified. Depending on the degree of spatial-filtering used in the Fourier-transform procedure, the presence of obstructions and blemishes can be easily overcome. An outline of the main procedure and a note on its application are presented here.

Begin with a raw phasemap $\phi(\mathbf{r})$ and one recorded interferogram $I(\mathbf{r})$ (which may be from of a series of interferograms).

> **Procedure 1: Fourier-Transform Guided Unwrap**
> 1. Apply the Fourier-transform method (Section 11.3) with *heavy filtering* to the interferogram $I(\mathbf{r})$. This produces a wrapped phasemap $\phi_\gamma(\mathbf{r})$.
> 2. Unwrap $\phi_\gamma(\mathbf{r})$ to produce the wavefront guide $\Gamma(\mathbf{r})$.
> 3. Apply guided unwrapping (Procedure 2b) to the raw data $\phi(\mathbf{r})$ using $\Gamma(\mathbf{r})$ as the guide.

Application Notes. Choosing the proper amount of spatial-filtering depends on three main attributes: the characteristics of the obscured regions, the amplitude and spatial-frequency of the noise present in the interferogram, and the curvature of the wavefront under test. With enough spatial filtering, isolated blemishes nearly vanish; even obstructions that cut the measurement domain into multiple disjoint sub-domains can be overcome, because the underlying phase can be made continuous across the blemishes and obscurations. When heavy filtering is applied, noise and other discontinuities are removed and unwrapping the guided wavefront becomes very simple. One cause for concern in the application of this method is the presence of highly-curved sections of the wavefront under test. Even in optical systems of high-quality, regions of high curvature may be present at the borders of the measurement domain as a result of diffraction. High-spatial-frequency components of small amplitude and low-spatial-frequency components of large amplitude are *both* attenuated by heavy filtering. The result may be a wavefront guide that fails to approximate the wavefront under test in some regions. The only straightforward solution in these cases is to relax the filtering until the problem is alleviated. It may occur, however, that the relaxation required to include all of the highly-curved wavefront components *undoes* the advantages that this method provides.

The problem of high wavefront curvature was identified in the discussion of single interferogram analysis (Chapter 11). High curvature violates the *monotonic phase requirement* described in Section 1.1.1 for single interferogram analysis and makes the application of filtering problematic. Hence the Fourier-Transform Guided Unwrapping Method is best suited to those cases for which the Fourier-transform methods of phase-retrieval are able to provide a low-spatial-frequency approximation to the wavefront under study. Where it is applicable, its strong advantages are that it is able to withstand isolated bad regions and discontinuities in the sub-region and to preserve the high-spatial-frequency content of the raw data without propagating phase-unwrapping errors throughout the data.

14

Aberration Polynomials

14.1 INTRODUCTION

Aberration polynomials are used to describe the continuous shape of the deformations of an optical wavefront, with respect to an ideal, often spherical, reference surface. While the shape of the aperture under study often dictates the appropriate set of polynomials, it is generally advantageous to use an *orthogonal* basis set. Such a set of polynomials not only enables the decomposition of a wavefront into experimentally meaningful constituent parts, but also facilitates numerical analysis of the measured data.

The most widely adopted representation for circular apertures is the basis set of *Zernike circular polynomials* Z_n^l of *n*-th degree (Zernike 1934, Zernike and Nijobar 1954). The Zernike polynomials are only orthogonal for circular apertures. Other polynomial sets include Zernike-Tatian (Fischer et al. 1993), Zernike-Mahajan (Mahajan 1994) for annular apertures, or Legendre polynomials for rectangular apertures.

This chapter presents the main representations of the aberration polynomials that are used to describe the interferometrically-measured wavefront data.

14.2 ZERNIKE POLYNOMIALS

Much has been written about the derivation and utility of the Zernike circular polynomials (several excellent references are Born and Wolf 1980:464-68, Malacara and deVore 1992, Carpio and Malacara 1994). This section presents, without proofs, only a brief overview of the most important aspects of the Zernike polynomials. There are many notation systems available for representing the Zernike polynomials; this chapter describes the notation used throughout this thesis.

The Zernike polynomials are obtained from the following two properties (Bathia and Wolf 1952, 1954; Born and Wolf 1980:464):

1. **Orthogonality.** The polynomials are orthogonal over the unit circle. Using the *Kronecker delta* symbol δ_{ij},

$$\int_0^1 \int_0^{2\pi} Z_n^l Z_{n'}^{l'*} \rho \, d\rho \, d\phi = \frac{\pi}{n+1} \delta_{nn'} \, \delta_{ll'} \, . \tag{1}$$

2. **Rotation.** The mathematical form of the polynomial is preserved when a rotation with a pivot at the center of the circle is applied to the function. By this property, the complex function Z_n^l may be separated into radial and azimuthal functions of the variables ρ and ϕ respectively, as follows:

$$Z_n^l = R_n^l(\rho)e^{il\phi} \, . \tag{2}$$

n is the degree of the polynomial, and *l* is the angular-dependence parameter. $|l|$ is the minimum exponent of the polynomials R_n^l. *n* and *l* are either both even or both odd; thus $n - l$ is always even.

The radial polynomials satisfy the relations:

$$R_n^l = R_n^{-l} = R_n^{|l|} \, . \tag{3}$$

$$\int_0^1 R_n^l R_{n'}^l \rho \, d\rho = \frac{1}{2(n+1)} \delta_{nn'} \, , \tag{4}$$

and can be generated by the expression

$$R_n^{n-2m}(\rho) = \sum_{s=0}^m (-1)^s \frac{(n-s)!}{s!(m-s)!(n-m-s)!} \rho^{n-2s} \, . \tag{5}$$

Since the azimuthal functions $e^{il\phi}$ are already orthogonal, any two R_n^l polynomials will be orthogonal if they do not have the same l.

A set of *real* polynomials Z_n^l may be written based on the complex U_n^l as

$$U_n^l = \begin{cases} \frac{1}{2}\left(Z_n^l + Z_n^{-l}\right) = R_n^l(\rho)\cos l\phi, & \text{for } l \le 0 \\ \frac{1}{2i}\left(Z_n^l - Z_n^{-l}\right) = R_n^l(\rho)\sin l\phi, & \text{for } l > 0 \end{cases} \tag{6}$$

$$\int_0^1 \int_0^{2\pi} U_n^l U_{n'}^{l'} \rho \, d\rho \, d\phi = \frac{\pi}{2(n+1)} \delta_{nn'} \, \delta_{ll'} \, . \tag{7}$$

satisfying the condition

Using the fact that $n \ge 0$ and $n - l$ is even, modify the definition of the azimuthal component of U_n^l to form U_n^m .

$$m \equiv \frac{n-l}{2} \, , \text{ or } \; l = n - 2m \, , \tag{8}$$

now

$$U_n^m = A_n^m R_n^{n-2m} \begin{Bmatrix} \sin \\ \cos \end{Bmatrix} (n - 2m)\phi \, . \tag{9}$$

where sine is used for $n - 2m > 0$ and cosine for $n - 2m \le 0$. With the addition of a convenient numbering system, these become the familiar Zernike polynomials.

14.3 NUMBERING CONVENTION AND COEFFICIENTS

Throughout the body of this text, the following conventions for the representation of Zernike polynomials are maintained.

• **Numbering convention.** An ordering system has been devised (Code V Reference Manual) to label the Zernike polynomials using a single, positive integer j to replace the pair $\{n, m\}$.

$$Z_j \to Z_n^m \, . \tag{10}$$

In the description of low-spatial-frequency optical aberrations, it is common to specify a set of 37 Zernike polynomials (0 through 36). The conventional ordering is shown in Table 1. Figure 1 shows a graphical representation of the first 37 Zernike polynomials.

Table 1: Single index notation for the Zernike polynomials.

j	*(n, m)*	*j*	*(n, m)*	*j*	*(n, m)*	*j*	*(n, m)*
0	(0, 0)	9	(3, 3)	18	(5, 3)	27	(6, 4)
1	(1, 1)	10	(3, -3)	19	(5, -3)	28	(6, -4)
2	(1, -1)	11	(4, 2)	20	(6, 2)	29	(7, 3)
3	(2, 0)	12	(4, -2)	21	(6, -2)	30	(7, -3)
4	(2, 2)	13	(5, 1)	22	(7, 1)	31	(8, 2)
5	(2, -2)	14	(5, -1)	23	(7, -1)	32	(8, -2)
6	(3, 1)	15	(6, 0)	24	(8, 0)	33	(9, 1)
7	(3, -1)	16	(4, 4)	25	(5, 5)	34	(9, -1)
8	(4, 0)	17	(4, -4)	26	(5, -5)	35	(10, 0)
						36	(12, 0)

• **Real quantities.** The polynomials described are *strictly real* quantities based on the set U_n^m from Eqns. (7) and (9). As described in the following sections, the symbol Z_j is used to represent individual, real, Zernike polynomials of the variables (ρ, ϕ), with $\rho \in [0, 1]$, and $\phi \in [0, 2\pi)$.

• **Leading coefficients.** There are two common conventions for the leading coefficients of the Zernike polynomials. Throughout this thesis, the leading coefficients of each Zernike polynomial are set to unity — not including the individual coefficients of the radial terms ρ^n that appear in each polynomial term. The Zernike polynomials are *bounded* on the range $[-1, 1]$. This convenient definition allows the immediate description of the magnitude of individual wavefront aberrations.

The second common convention in use sets the leading coefficients equal to the *variances* of the individual terms (excluding the constant *piston* term.) That is, Z_j is defined with a leading coefficient that satisfies

$$\left(Variance_{\mathrm{j}}\right)^2 = \sigma_j^2 = \int_0^1 \int_0^{2\pi} Z_j^2 \, \rho \, d\rho \, d\phi \quad . \tag{11}$$

Although this definition simplifies the calculation of wavefront variance when the Zernike coefficients are known, it complicates the rapid interpretation of aberration magnitudes by the inclusion of (*mathematically*) irrational coefficients in each term.

14.3.1 *Vector Representation of Zernike Coefficient Pairs*

In several circumstances, pairing Zernike polynomials that share the same radial dependence is extremely useful in the concise representation of wavefront aberrations. This is especially true in the description of systematic errors (Chapters 5 and 8) where the rotational orientation of a given effect is independent of the coordinate system used for measurement. Throughout this thesis, a vector notation for *coefficient pairing* is utilized.

For example, wavefront *tilt* and *coma* are represented by the coefficient pairs (a_1, a_2) and (a_6, a_7) of the Zernike series respectively. In both cases, the two Zernike polynomials they modify have have $\cos\theta$ dependence in the first term and $\sin\theta$ dependence in the second term. This lends itself to a simple vector notation as follows

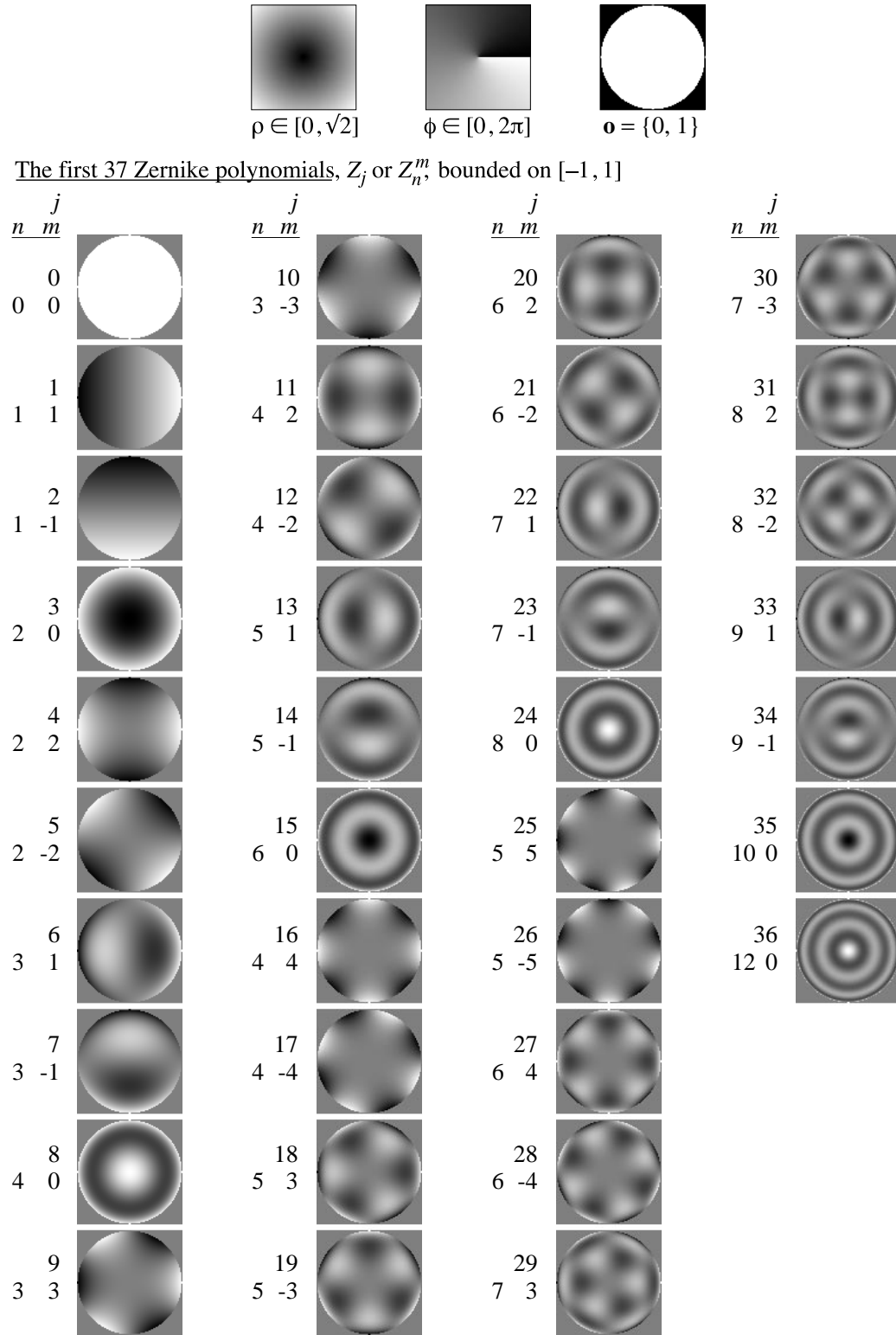$$\text{Tilt, } \mathbf{T} \equiv (a_1, a_2), \text{ and Coma, } \mathbf{C} \equiv (a_6, a_7). \tag{12}$$

$\rho \in [0, \sqrt{2}]$ $\phi \in [0, 2\pi]$ $\mathbf{o} = \{0, 1\}$

The first 37 Zernike polynomials, Z_j or Z_n^m, bounded on $[-1, 1]$

Figure 1. A graphical representation of the first 37 Zernike polynomials (0 through 36) and the three square arrays used to generate them. ρ is the radius array, ϕ is the azimuthal angle defined counter-clockwise from the x-axis, and $\mathbf{o}$ is the binary sub-domain-defining array which represents the unit circle on the rectangular grid. Points outside of the sub-domain are undefined. Adjacent to each Zernike term are the two-index and the single-index representations.

231

14.4 WAVEFRONT REPRESENTATION WITH THE VECTOR NOTATION

A wavefront $W(\rho, \phi)$ may be represented by a finite set of $(M+1)$ Zernike polynomials.

$$W(\rho,\phi) = \sum_{j=0}^{M} a_j Z_j(\rho,\phi) \,. \tag{13}$$

On a discrete set of N points $\{\boldsymbol{\rho}_n\}$ or $\{(\rho_n, \phi_n)\}$ in an aperture domain A, for each point we have

$$W(\boldsymbol{\rho}_n) \equiv W_n = \sum_{j=0}^{M} a_j Z_j(\boldsymbol{\rho}_n) \,. \tag{14}$$

A more compact *vector notation* describes a point in the wavefront at position $\boldsymbol{\rho}_n$ as a vector on a basis of Zernike polynomials.

$$W_n = \begin{bmatrix} a_0 & \cdots & a_M \end{bmatrix} \begin{bmatrix} Z_0(\boldsymbol{\rho}_n) \\ \vdots \\ Z_M(\boldsymbol{\rho}_n) \end{bmatrix}, \text{ or equivalently, } W_n = \begin{bmatrix} Z_0(\boldsymbol{\rho}_n) & \cdots & Z_M(\boldsymbol{\rho}_n) \end{bmatrix} \begin{bmatrix} a_0 \\ \vdots \\ a_M \end{bmatrix} . \tag{15}$$

On the finite set of N points $\{\boldsymbol{\rho}_n\}$, the wavefront W_n may be written as a column vector. Equation (15) becomes

$$\begin{bmatrix} W_1 \\ \vdots \\ W_N \end{bmatrix} = \begin{bmatrix} Z_0(\boldsymbol{\rho}_1) & \cdots & Z_M(\boldsymbol{\rho}_1) \\ \vdots & & \vdots \\ Z_0(\boldsymbol{\rho}_N) & \cdots & Z_M(\boldsymbol{\rho}_N) \end{bmatrix} \begin{bmatrix} a_0 \\ \vdots \\ a_M \end{bmatrix} . \tag{16}$$

The dimension of the matrix in Eq. (16) is $M \times N$.

Within this notation, there are now several "vectors" we can define: the wavefront $\mathbf{W}$ has a value for each point in the domain; each Zernike polynomial term $\mathbf{Z}_j$ may be represented as a vector across the domain; for a given domain, there is a vector $\mathbf{Z}^M$ defined on the finite Zernike polynomial basis, spanning the space defined by the first $M+1$ polynomials; and there is a coefficient vector $\mathbf{a}$ of $M+1$ elements.

$$\mathbf{W} \equiv \begin{bmatrix} W_1 & \cdots & W_N \end{bmatrix}, \tag{17a}$$

$$\mathbf{Z}_j \equiv \begin{bmatrix} Z_j(\boldsymbol{\rho}_1) \cdots Z_j(\boldsymbol{\rho}_N) \end{bmatrix}, \text{ and } \hat{\mathbf{Z}} \equiv \begin{bmatrix} Z_0(\boldsymbol{\rho}_1) & \cdots & Z_M(\boldsymbol{\rho}_1) \\ \vdots & & \vdots \\ Z_0(\boldsymbol{\rho}_N) & \cdots & Z_M(\boldsymbol{\rho}_N) \end{bmatrix} = \begin{bmatrix} \mathbf{Z}_0 & \cdots & \mathbf{Z}_M \end{bmatrix}, \tag{17b}$$

$$a \equiv \begin{bmatrix} a_0 & \cdots & a_M \end{bmatrix} . \tag{17c}$$

Several of the above expressions may now be re-written in this compact vector form. The wavefront representation from Eq. (16) becomes

$$\mathbf{W}^T = \hat{\mathbf{Z}}\mathbf{a}^T, \text{ or } \mathbf{W} = \mathbf{a}\hat{\mathbf{Z}}^T \,. \tag{18}$$

As usual, the superscript T indicates the transpose of a vector or matrix. In the conventional notation, the orthogonality condition is

$$\sum_{n=0}^{N} Z_j(\mathbf{\rho}_n) Z_k(\mathbf{\rho}_n) \propto \delta_{jk} \, . \tag{19}$$

In vector notation, the orthogonality condition may be written as

$$\mathbf{Z}_j \mathbf{Z}_k^T \propto \delta_{jk} \, . \tag{20}$$

To study the variance of a given fit (Chapter 15), we require the definition of a *vector norm* across the set of *N* measured points.

$$\|\mathbf{W}\|^2 = \sum_{n=1}^{N} W_n^2 = \mathbf{W}\mathbf{W}^T \, . \tag{21}$$

14.5 REPRESENTATION OF THE ZERNIKE POLYNOMIALS ON A SQUARE GRID DOMAIN

The first step in the analysis of a digitized wavefront must be the establishment of a consistent coordinate system used in all stages of the analysis. Modern detector designs make the establishment of a rectangular Cartesian coordinate system a natural choice. Appropriate to the Zernike polynomials on a circular aperture will be a representation of the *unit circle* within the chosen domain. However, *any* contiguous or disjointed domain(s) of points may be used once an appropriate coordinate system has been established. This step may appear trivial, but there are subtleties in the procedure worthy of discussion. Carpio and Malacara (1993) have suggested a method of representing the Zernike polynomials in Cartesian coordinates. The method described here uses a direct representation of the polar coordinates on a square-grid domain.

Beginning with a square $N \times N$ domain of points *D,* our goal is to establish three array variables shared by all analysis procedures: $\mathbf{\rho}$, $\mathbf{\phi}$, and $\mathbf{o}$. For each point in *D*, $\mathbf{\rho}$ is the distance from the center, $\mathbf{\phi}$ is an azimuthal angle defined counter-clockwise from the *x*-axis, and $\mathbf{o}$ is a binary array describing which points are in the unit circle ($o = 1$) and which points lie outside ($o = 0$). As an intermediate step, define the array variables $\mathbf{x}$ and $\mathbf{y}$ in the following way. These array variables are linear and are bounded on the range [–1, 1].

$$\begin{cases} \mathbf{x}(1,*) = -1, & \mathbf{x}(N,*) = 1 \\ \mathbf{y}(*,1) = -1, & \mathbf{y}(*,N) = 1 \end{cases} . \tag{22}$$

Here * represents all columns (or rows) from 1 to *N*. $\mathbf{x}$ and $\mathbf{y}$ are shown in Figure 2 for an 8×8 array. This very small array is used only to illustrate the method; the EUV interferograms studied in this thesis actually occupy domain sizes from 225×225 to 860×860 pixels.

Many computer programming environments are capable of correctly rendering an arctangent into all four quadrants, using both *x* and *y* as input arguments, and yielding an angle modulo 2π. Computer systems without such capacity use the *ratio* of *y* to *x* as a single input argument and angles are returned modulo π, because sign information is lost in the division. In either case, $\mathbf{\phi}$ should be defined in the straightforward
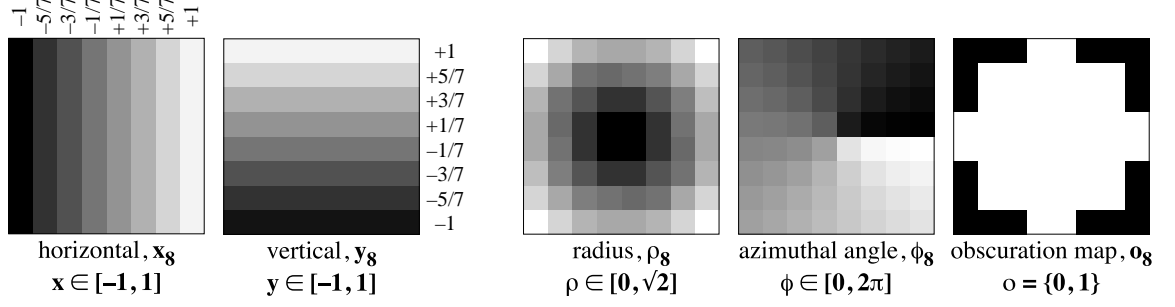
233

Figure 2. Definition of ρ and ϕ proceeds from the definition of the intermediate arrays **x** and **y**, illustrated in this example of an 8×8 square grid domain. In experimental applications, these arrays are typically hundreds of elements wide and contain tens of thousands of domain points.

manner, on the range $[0, 2\pi]$.

$$\phi = \tan^{-1}(\mathbf{y}, \mathbf{x}), \quad \text{typical modulo } 2\pi \text{ format },\tag{23a}$$

$$\phi = \tan^{-1}\left(\frac{\mathbf{y}}{\mathbf{x}}\right), \quad \text{alternate modulo } \pi \text{ format }.\tag{23b}$$

The definition of ρ requires the most care. The most simple definition of ρ is

$$\rho = \sqrt{\mathbf{x}^2 + \mathbf{y}^2} .\tag{24}$$

This definition will be modified below for *even-N* arrays, .

It is very important to decide *where* the coordinate of a point resides within each square pixel. For symmetry reasons, we choose the *center of the square* as the locus of its coordinates. This choice maintains both 90° rotational symmetry and reflection symmetry about the two axes, but affects odd- and even-sized arrays differently.

One fact is immediately:apparent in the even-N case there is no single pixel corresponding to the origin, and no individual row or column corresponding to the *x*- or *y*-axis. This difference from the *odd-N* case does not affect measurements in any significant way.

Proper treatment of the points at the edges of the domain is the most important aspect of the definition of ρ. With **o** defined as

$$o = \begin{cases} 1, & \rho \leq 1 \\ 0, & \rho > 0 \end{cases},\tag{25}$$

care must be taken to ensure that the non-zero points of **o** extend to the edges of the domain. Based solely on Eqns. (24) and (25), this condition would not be met for the even-N arrays. The two points at the center of any side have $\rho > 1$ and would be excluded, leaving empty rows and columns along each edge. The following "fix" compensates for this problem by adjusting the definition of ρ for even-N arrays:

$$\text{IF } N \text{ is even THEN } \rho' \equiv \frac{\rho}{\max\{\rho(*,0)\}} .\tag{26}$$

234

After this normalization, with **ρ** redefined as **ρ′**, the maximum value of **ρ** along the edges is identically *one.*

To illustrate the differences between the even and odd array definitions, Fig. 3 shows the appearance of **o** for an 8 × 8 and a 9 × 9 domain. After applying the "renormalization" of Eq. (26) to the even-sized array, the included points of **o** (that is, the non-zero points) reach the edges of the domain.

14.5.1 *Note on Distortion*

The definition of the coordinate system variables **ρ** and **ϕ** presents an opportunity to include compensation for some geometrical systematic errors directly in the analysis. For example, the radial distortion related to the geometry of a planar detector array in a spherical beam (Section 5.12) can, in principle, be compensated for *automatically* by re-defining the radial coordinate **ρ**. In

ideal representation

discretized

Even (8 × 8)   Odd (9 × 9)

Figure 3. The definition of the radius array **ρ** depends critically on how the unit circle is defined, and care must be taken to ensure proper behavior at the edges of the domain. This figure illustrates how the ideal representation translates into symmetric even-sized and odd-sized discrete domains. It is important for the domain points to reach the edges of the domain at the points where **ρ** = 1. This condition is guaranteed for even-sized arrays by making the modification in Eq. (26).

this particular case, a radial position ρ in the *Detector Coordinate System* corresponds to a polar angle γ(ρ) in the spherical *Beam Coordinate System.* By replacing ρ with γ(ρ) in the coordinate system definition, all measurements will automatically be made in the Beam Coordinate System.

This treatment is not required; coordinate transformations can be done after the data has been analyzed. However, this process can be simplified by building the transformation into the radial coordinate. This is especially true of the representation of a measured wavefront using the Zernike polynomial series, in which a coordinate *and coefficient* transformation in the presence of a non-linear radius is challenging.
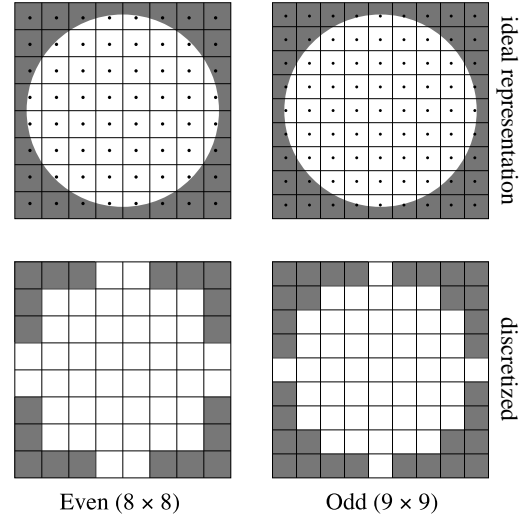
15

Wavefront Surface Fitting

15.1 INTRODUCTION

Once the raw interferogram data has been processed and an unwrapped wavefront phasemap has been produced, the wavefront may be interpreted as the composition of individual, constituent wavefront aberrations. Reconstruction of the raw wavefront data from a limited number of these constituent aberrations also serves as a method of filtering the data to contain only the lowest-spatial-frequency components. The goal of this chapter is to describe several methods of wavefront analysis leading to the development of a novel, expedient variation of a well-established polynomial fitting technique.

The conventional measure of the *goodness of a fit* is based on the minimization of the function χ^2, defined as the ratio of the estimated variance to the parent variance times the number of degrees of freedom ν (Bevington 1969:188). The parent variance is characteristic of the spread of the data about the parent distribution, for which the estimated variance of the fit describes both the spread of the data and the precision of the fit.

The individual uncertainty of *each* individual data point σ_n is included in the definition of χ^2. This fact adds *significant* complication to wavefront surface fitting computations if simplifying assumptions are not made. For instance, the basis set of orthogonal polynomials on the measurement domain must be defined to be orthogonal in the presence of a non-uniform weighting function based on these individual uncertainties.

One simplifying assumption that is often appropriate in interferogram analysis is that the uncertainties of the phase measurements are equal to a constant σ across the measurement domain. (The domain is defined to include only valid data points.) Where this assumption is applicable, the function χ^2 is simply proportional to the fit variance *(*defined in the following section). Thus the method of wavefront surface fitting described in this chapter is essentially a minimization of the fit variance, based on the raw wavefront data and an appropriate basis set of aberration polynomials. This chapter describes methods that are general and may be applied to the orthogonalization of any arbitrary set of basis polynomials on a given domain.

15.1.1 *Note on Numbering Conventions*

For consistency with the Zernike polynomial basis, all polynomial basis "vectors" are numbered starting from 0; that is, X_0 is the "first" polynomial of an arbitrary basis. When polynomials up to and including X_M are used, then there are $M+1$ basis vectors. In regard to the Zernike basis, typically polynomials Z_0 through Z_{36} are used to describe aberrations in imaging systems. These constitute the well-known "first 37 Zernike polynomials."

However, on the discrete *measurement* domain, the N measured data points are numbered from 1 to N. Thus, the position vectors $\boldsymbol{\rho}_1$ through $\boldsymbol{\rho}_N$ describe the measurement domain.

15.2 MINIMIZING THE FIT VARIANCE

The process of wavefront surface fitting described here is based on minimization of the *fit variance*. The fit variance is defined for a measured wavefront $\mathbf{W}$ and a fit $\mathbf{W}'$ based on an arbitrary, *finite* set of basis polynomials $\{\mathbf{X}_j\}$. The chosen set $\{\mathbf{X}_j\}$ may be any convenient set and need not be orthogonal. The following discussion is based on the method described by Fischer et al. (1993), and uses the vector notation described in Chapter 14.

In general, surface fitting on a basis of polynomial functions may be represented as

$$\mathbf{W}' = \sum_{j=0}^{M} c_j \mathbf{X}_j = \mathbf{c}\hat{\mathbf{X}}^T . \tag{1}$$

The individual vectors $\mathbf{X}_j$ range over the set of N measurement points. The set $\{c_j\}$ are the scalar polynomial coefficients and form the elements of the coefficient vector $\mathbf{c}$. Over a discrete domain, where the fit variance is defined (Bevington 1969:137) as

$$s^2 \equiv \frac{1}{N-M-1}\sum_{n=1}^{N}\left(W_n' - W_n\right)^2 = \frac{1}{N-M-1}\left\|\mathbf{W}' - \mathbf{W}\right\|^2 . \tag{2}$$

N is the number of points in the measurement domain, and $(M+1)$ is the number of parameters used in the fit $\mathbf{W}'$.

Inserting the wavefront fit of Eq. (1) into Eq. (2), we define for convenience a scalar quantity S proportional to the variance (and also proportional to χ^2):

$$S = (N-M-1)s^2\left\|\mathbf{c}\hat{\mathbf{X}}^T - \mathbf{W}\right\|^2 . \tag{3}$$

The minimization of s^2 (or, analogously, of S) is based on the selection of the optimum set of coefficients $\mathbf{c}$. If a perfect fit were possible, S would equal zero. Since there will always be a difference between the measured wavefront and the wavefront reconstructed from the fit, S will be non-zero. The optimization thus requires finding a global minimum of S with respect to each coefficient c_k. This minimum occurs when the partial derivative of S with respect to each c_k is zero.

$$0 = \frac{\partial S}{\partial c_k} = \frac{\partial}{\partial c_k}\left\|\mathbf{c}\hat{\mathbf{X}}^T - \mathbf{W}\right\|^2 = 2\left(\mathbf{c}\hat{\mathbf{X}}^T - \mathbf{W}\right)\mathbf{X}_k^T . \tag{4}$$

Thus, for each k,
$$\mathbf{c}\hat{\mathbf{X}}^T\mathbf{X}_k^T = \mathbf{W}\mathbf{X}_k^T . \tag{5}$$

Equation (5) may be generalized for all k as follows:

$$\mathbf{c}\hat{\mathbf{X}}^T\hat{\mathbf{X}} = \mathbf{W}\hat{\mathbf{X}}, \quad \text{or} \quad \sigma^2\mathbf{c}\boldsymbol{\alpha} = \mathbf{W}\hat{\mathbf{X}} . \tag{6a}$$

using the definition
$$\boldsymbol{\alpha} \equiv \frac{1}{\sigma^2}\hat{\mathbf{X}}^T\hat{\mathbf{X}} . \tag{6b}$$

As described earlier, σ is the (uniform) uncertainty of each data point in the measured wavefront. The symmetric matrix $\boldsymbol{\alpha}$ is called the *curvature matrix* because it is related to the curvature of S (or s^2, or χ^2) in coefficient space. For clarity, Eq. (6a) may be expanded and re-arranged in matrix form:

$$\begin{bmatrix} \mathbf{X}_0\mathbf{X}_0^T & \cdots & \mathbf{X}_M\mathbf{X}_0^T \\ \vdots & & \vdots \\ \mathbf{X}_0\mathbf{X}_M^T & \cdots & \mathbf{X}_M\mathbf{X}_M^T \end{bmatrix} \begin{bmatrix} c_0 \\ \vdots \\ c_M \end{bmatrix} = \begin{bmatrix} \mathbf{W}\mathbf{X}_0^T \\ \vdots \\ \mathbf{W}\mathbf{X}_M^T \end{bmatrix}. \tag{7}$$

It is important to note that the curvature matrix has *no dependence* on the measured data. The matrix depends on the *domain* of the data, but not on the measured values. The measurements are contained in $\mathbf{W}$, on the right-hand-side of Eqns. (5) through (7). This fact may be exploited to improve computational efficiency in situations where many separate wavefront measurements are performed on the same domain.

Solving for $\mathbf{c}$ may proceed in one of three ways. One way is to assume that the polynomials $\{\mathbf{X}_j\}$ are orthogonal. If there are enough sampled points in the domain, this may be a good approximation; but it can introduce significant errors, especially for the coefficients of the higher-ordered polynomial terms. A second method requires the inversion of the curvature matrix. Great care must be taken because such inversions are notoriously ill-conditioned (Conte and de Boor 1980:249) and therefore extremely sensitive to small changes in the input conditions. The third and most sound method is to perform a transformation to a polynomial basis that is orthogonal over the domain, where the curvature matrix becomes diagonal, and makes solution straightforward. This third approach is typically accomplished using the Gram-Schmidt method (Wang and Silva 1980, Fischer et al. 1993). All three methods are discussed in detail in the following sections; error estimation is discussed in Section 15.6.

15.3 ORTHOGONAL BASIS ASSUMPTION

The minimization problem is particularly simple when the polynomials $\{\mathbf{X}_j\}$ are orthogonal over the measurement domain. The curvature matrix in Eq. (7) becomes diagonal, and the solution is

$$\mathbf{c} = \begin{bmatrix} \dfrac{\mathbf{W}\mathbf{X}_0^T}{\|\mathbf{X}_0\|^2} & \cdots & \dfrac{\mathbf{W}\mathbf{X}_M^T}{\|\mathbf{X}_M\|^2} \end{bmatrix}. \tag{8}$$

This is essentially the *projection* of the measured data $\mathbf{W}$ onto the orthogonal basis set. This approach requires the fewest calculations, and computationally may be the fastest method to perform.

When the discretized domain is a close approximation to an unobstructed circular aperture and when only the lowest-ordered terms are of interest, this method may work quite well. However, experience has shown that significant errors should be expected for certain polynomial terms. We here define a given term as *unbalanced* if the sum (or integral) of the term over the domain is not zero; equivalently, such a term

fails to meet the orthogonality condition that its scalar product with the (constant) *piston* term is zero.

$$\mathbf{Z}_j\mathbf{Z}_0^T \neq 0, \text{ or } \sum_{n=1}^{N} Z_j(\boldsymbol{\rho}_n) \neq 0, \text{ when } j \neq 0 \implies \mathbf{Z}_j \text{ is unbalanced .} \tag{9}$$

For example, consider a measured wavefront $\mathbf{W}$ consisting only of a non-zero constant (piston) over the domain. The solution of $\mathbf{c}$ in Eq. (8) would yield erroneous, non-zero coefficients for any term that is unbalanced.

Specific polynomials that routinely cause difficulty are the cylindrically symmetric terms (defocus, spherical aberration, etc.) and those with 3θ or 5θ angular dependence. Because they do not match the symmetry of the rectangularly gridded domain, these terms are usually unbalanced. Over an unobstructed and symmetric aperture, the terms with θ or 2θ angular dependence (tilt, astigmatism, and coma) *are* usually balanced and orthogonal because they match the symmetry of the domain.

15.4 MATRIX INVERSION METHOD

To solve for $\mathbf{c}$ using matrix inversion, post-multiply both sides of Eqns. (6b) or (7) by the inverse of the matrix on the left-hand-side (the curvature matrix):

$$\mathbf{c} = \mathbf{W}\hat{\mathbf{X}}\left(\hat{\mathbf{X}}^T\hat{\mathbf{X}}\right)^{-1}, \text{ or } \mathbf{c} = \sigma^2\mathbf{W}\hat{\mathbf{X}}\boldsymbol{\varepsilon}, \tag{10}$$

using the definition

$$\boldsymbol{\varepsilon} \equiv \boldsymbol{\alpha}^{-1} = \left(\frac{1}{\sigma^2}\hat{\mathbf{X}}^T\hat{\mathbf{X}}\right)^{-1} = \sigma^2\left(\hat{\mathbf{X}}^T\hat{\mathbf{X}}\right)^{-1}. \tag{11}$$

The inverse $\boldsymbol{\varepsilon}$ of the curvature matrix $\boldsymbol{\alpha}$ is also a symmetric matrix. This matrix is called the *error matrix* for its role in error estimation, described in Section 15.6.

The reliability of the matrix inversion must be determined on a case-by-case basis. Great care must be taken to ensure that the matrix is not ill-conditioned. Experience has shown that the matrix inversion methods are typically unreliable, owing primarily to the fact that the aberration polynomials, defined on the discrete domain, are not orthogonal. The presence of these *unbalanced* polynomials leads to non-zero off-diagonal elements in $\hat{\mathbf{X}}^T\hat{\mathbf{X}}$, making the matrix ill-conditioned.

15.5 GRAM-SCHMIDT METHODS OF ORTHOGONALIZATION

Beginning with a convenient set of M arbitrary polynomials on the measurement domain $\{\mathbf{X}_j\}$, the goal is to find an orthogonal basis set of M polynomials $\{\mathbf{Y}_j\}$ and the transformation matrix between the two. A measured wavefront is fit on the orthogonal polynomial basis to reduce the uncertainties in the fitting procedure. Often, the orthogonal set $\{\mathbf{Y}_j\}$ is only used as an intermediate part of the wavefront fitting and the final results are given as a coefficient vector $\mathbf{c}$ defined on the convenient basis $\{\mathbf{X}_j\}$.

> {$\mathbf{X}_j$} *convenient* basis $\mathbf{c}$ coefficient vector in $\mathbf{X}$-space.
> {$\mathbf{Y}_j$} *orthogonal* basis, calculated from{$\mathbf{X}_j$} $\mathbf{b}$ coefficient vector in $\mathbf{Y}$-space.

The Gram-Schmidt method of basis orthogonalization is recursive: each successive polynomial $\mathbf{Y}_j$ is added to the previous (j-1) polynomials in such a way that all of the terms {$\mathbf{Y}_j$} are mutually orthogonal. Each $\mathbf{Y}_j$ begins with $\mathbf{X}_j$. Then a linear combination of the previous polynomials is found such that subtraction from $\mathbf{X}_j$ yields a new orthogonal polynomial.

It is worth reiterating that the new set of polynomials and the accompanying transformation matrix are determined only by the *domain* of the data, and not by the measured wavefront. While the determination of the new basis may be computationally intensive, this basis set and transformation matrix may be calculated once and stored for future, rapid application to a series of related measurements.

Two Gram-Schmidt methods are presented here, differing only in the way the transformation matrix is determined. In both, the transformation matrix is developed in parallel with the calculation of the new orthogonal set: the individual projections become the elements of the transformation matrix. The method which appears in the literature (Wang and Silva 1980, Fischer et al. 1993) requires that this lower-triangular transformation matrix be inverted (typically by the method of back-substitution) to determine the coefficients of the *original* polynomials from those of the *new* orthogonal polynomials. In a new, more efficient approach introduced here (Section 15.5.2), the projections are used to develop the inverted matrix *directly*.

15.5.1 *Gram-Schmidt: Conventional Method*

The orthogonalization process begins with the definition

$$\mathbf{Y}_0 \equiv \mathbf{X}_0 . \tag{12}$$

Then each successive term $\mathbf{Y}_j$ is projected onto the new basis and the subtraction of this projection from $\mathbf{X}_j$ yields a new orthogonal polynomial; the individual projections become the elements of a transformation matrix.

$$\mathbf{Y}_j = \mathbf{X}_j - \sum_{s=0}^{j-1} \frac{\mathbf{X}_j \mathbf{Y}_s^T}{\mathbf{Y}_s \mathbf{Y}_s^T} \mathbf{Y}_s = \mathbf{X}_j - \sum_{s=0}^{j-1} \frac{\mathbf{X}_j \mathbf{Y}_s^T}{\left\| \mathbf{Y}_s \right\|^2} \mathbf{Y}_s, \ \ j > 0 . \tag{13}$$

The off-diagonal elements of this transformation matrix may be read directly from Eq (13), as the scalar coefficients of $\mathbf{Y}_s$. As an intermediate step we define the matrix $\mathbf{D}$, with off-diagonal elements D_{js}.

$$D_{js} \equiv \frac{\mathbf{X}_j \mathbf{Y}_s^T}{\left\| \mathbf{Y}_s \right\|^2} , \ j > s . \tag{14}$$

242

This allows us to write
$$\mathbf{Y}_j \equiv \mathbf{X}_j - \sum_{s=0}^{j-1} D_{js} \mathbf{Y}_s . \tag{15}$$

These two basis sets form equivalent representations of an arbitrary wavefront $\mathbf{W}'$,.

$$\mathbf{W}' = \mathbf{c}\hat{\mathbf{X}}^T = \mathbf{b}\hat{\mathbf{Y}}^T . \tag{16}$$

Since the set of polynomials $\{\mathbf{Y}_j\}$ is orthogonal, we may apply Eq. (8) to find $\mathbf{b}$, substituting $\mathbf{b}$ for $\mathbf{c}$ and $\mathbf{Y}_j$ for $\mathbf{X}_j$,

$$\mathbf{b} = \left[\frac{\mathbf{W}\mathbf{Y}_0^T}{\|\mathbf{Y}_0\|^2} \quad \cdots \quad \frac{\mathbf{W}\mathbf{Y}_M^T}{\|\mathbf{Y}_M\|^2} \right] . \tag{17}$$

Finding the coefficients $\mathbf{c}$ requires back-substitution. Beginning with Eq. (16) in matrix form,

$$\begin{bmatrix} \mathbf{Y}_0 \\ \vdots \\ \mathbf{Y}_M \end{bmatrix} = \begin{bmatrix} \mathbf{X}_0 \\ \vdots \\ \mathbf{X}_M \end{bmatrix} - \begin{bmatrix} 0 & \cdots & & & 0 \\ D_{10} & 0 & \cdots & & 0 \\ D_{20} & D_{21} & 0 & \cdots & 0 \\ \vdots & \vdots & & \ddots & \\ D_{M0} & D_{M1} & \cdots & D_{MM-1} & 0 \end{bmatrix} \begin{bmatrix} \mathbf{Y}_0 \\ \vdots \\ \mathbf{Y}_M \end{bmatrix} , \tag{18a}$$

$$\hat{\mathbf{Y}}^T = \hat{\mathbf{X}}^T - \mathbf{D}\hat{\mathbf{Y}}^T . \tag{18b}$$

Using $\mathbf{D}$ to represent the matrix with the elements D_{js} and $\mathbf{I}$ as an $M \times M$ identity matrix, Eq. (18b) can be solved for $\mathbf{Y}$:

$$\hat{\mathbf{Y}}^T = (\mathbf{I} + \mathbf{D})^{-1}\hat{\mathbf{X}}^T \equiv \mathbf{G}\hat{\mathbf{X}}^T . \tag{19a}$$

Here, the transformation matrix $\mathbf{G}$ is defined as

$$\mathbf{G} \equiv (\mathbf{I} + \mathbf{D})^{-1} . \tag{19b}$$

Substituting Eq. (19a) into Eq. (16), the coefficients are related by

$$\mathbf{c} = \mathbf{b}(\mathbf{I} + \mathbf{D})^{-1} = \mathbf{b}\mathbf{G} . \tag{20}$$

Here again, care must be taken in the inversion to ensure that the matrix is not ill-conditioned.

15.5.2 *A More Expedient Method*

A more expedient method proceeds in the same way as the Conventional Method, presented above. The difference is in the way the transformation matrix is developed from the projections. The transformation matrix $\mathbf{G}$ enables us to determine the orthogonal polynomials $\{\mathbf{Y}_j\}$ from the arbitrary set $\{\mathbf{X}_j\}$, and also provides a means to rapidly transform coefficients of $\{\mathbf{Y}_j\}$ to coefficients of $\{\mathbf{X}_j\}$. The definition and utility of $\mathbf{G}$ are shown in Eqns (19) and (20). Expanding Eq. (19a) into a summation,

$$\mathbf{Y}_j = \sum_{m=0}^{M} G_{mj}\mathbf{X}_m . \tag{21}$$

243

To begin, the first polynomials of each basis are made equivalent, as before. The first diagonal matrix element G_{00} is set to 1 to reflect this equality.

$$\mathbf{Y}_0 \equiv \mathbf{X}_0. \tag{22}$$

$$G_{00} = 1. \tag{23}$$

Recursively, as before, the next polynomials $\mathbf{Y}_{j>1}$ are formed from $\{\mathbf{X}_s\}$, subtracting the projection of $\mathbf{X}_j$ onto the previously calculated $\{\mathbf{Y}_{s<j}\}$.

$$\mathbf{Y}_j = \mathbf{X}_j - \sum_{s=0}^{j-1} \frac{\mathbf{X}_j \mathbf{Y}_s^T}{\mathbf{Y}_s \mathbf{Y}_s^T} \mathbf{Y}_s = \mathbf{X}_j - \sum_{s=0}^{j-1} \frac{\mathbf{X}_j \mathbf{Y}_s^T}{\|\mathbf{Y}_s\|^2} \mathbf{Y}_s, \quad j > 0. \tag{24}$$

However, since we are interested in keeping the expression in terms of $\{\mathbf{X}_j\}$, we substitute the previously calculated $\mathbf{Y}_s$ into Eq. (24), as follows:

$$\mathbf{Y}_j = \mathbf{X}_j - \sum_{s=0}^{j-1} \frac{\mathbf{X}_j \left(\sum_{t=0}^{s} \frac{G_{st} \mathbf{X}_t}{\|\mathbf{X}_t\|^2} \right)^T}{\|\mathbf{Y}_s\|^2} \left(\sum_{t=0}^{s} \frac{G_{st} \mathbf{X}_t}{\|\mathbf{X}_t\|^2} \right), \quad j > 0. \tag{25}$$

$\|\mathbf{Y}_s\|^2$ is simply a constant that can be calculated once for each s. While on paper this may look *more* complicated than the Conventional Method, it is in fact very straightforward to implement in a computer program. Utilizing matrix row-arithmetic, we have a procedure as follows.

Performing row-arithmetic (Step 6) as the $\{\mathbf{Y}_j\}$ polynomials are calculated enables us to calculate the transformation matrix directly, without subsequent back-substitution. To improve computational efficiency, the norm of each of the polynomials $\mathbf{Y}_s$ should be calculated only once and stored for repeated future use.

For wavefront fitting, the coefficients $\mathbf{b}$ of $\{\mathbf{Y}_j\}$ are determined as before, from Eq. (17). Now, the computation of the coefficients $\mathbf{c}$ of $\{\mathbf{X}_j\}$ requires *no matrix inversion*. Since $\mathbf{G}$ is determined directly, from the orthogonalization procedure, Eq. (19a) can be used to compute the orthogonal basis polynomials from the original basis and Eq. (20) allows the coefficients of $\{\mathbf{X}_j\}$ to be determined from the coefficients of $\{\mathbf{Y}_j\}$.

Procedure: Expedient Gram-Schmidt Orthogonalization

1. $G_{00} \equiv 1$
2. Loop j from 1 to M
3. $G_{jj} \equiv 1$
4.   Loop s from 0 to $(j-1)$
5. $\mathbf{Y}_s = [\mathbf{G}]_{\text{row } s} \hat{\mathbf{X}}^T$
6. $[G]_{row\,j} \leftarrow [G]_{row\,j} - \dfrac{\mathbf{X}_j \mathbf{Y}_s^T}{\|\mathbf{Y}_s\|^2} [G]_{row\,s}$

15.6 WAVEFRONT FITTING ERROR ANALYSIS

In general, interferogram wavefront surface fitting error analysis proceeds along several fronts. One goal is to describe the success of a reconstructed-wavefront fit in accurately representing the raw data. A second issue is specifying the agreement among a series of similar measurements, and third is understanding the inherent limitations on the measurement precision, based on the known or measured uncertainties in each element of the system. This particular section addresses only the quality of the polynomial wavefront fitting, based on a measured wavefront phasemap and a given or a calculated basis of polynomial functions. First, the general approach, applicable to any of the previously described methods, will be explained; the error estimation is significantly simplified in those analysis methods that employ the Gram-Schmidt orthogonalization.

The most convenient starting point is to determine the uncertainties in the fitting coefficients **b** of the orthogonal basis $\{\mathbf{Y}_j\}$. Following the conventional method of error propagation with Gaussian error distributions, the estimated uncertainty $\sigma_{b_j}^2$ in an individual fitting coefficient b_j is given by a sum of squares of the individual uncertainty contributions of each point in the measurement domain.

$$\sigma_{b_j}^2 = \sum_{n=1}^{N}\left[\sigma_n^2\left(\frac{\partial b_j}{\partial W_n}\right)^2\right] = \sigma^2 \sum_{n=1}^{N}\left(\frac{\partial b_j}{\partial W_n}\right)^2 . \tag{26}$$

σ_n is the estimated uncertainty in the measurement of an individual wavefront point. By a previous assumption (Section 15.1), the individual uncertainties are considered to be equivalent and equal to σ over the domain of valid data points. The partial derivative may be evaluated from Eq. (10), modified for **b** and $\hat{\mathbf{Y}}^T$. Here $\boldsymbol{\varepsilon}$ is evaluated for $\{\mathbf{Y}_j\}$, the basis under consideration.

$$\mathbf{b} = \mathbf{W}\hat{\mathbf{Y}}\left(\hat{\mathbf{Y}}^T\hat{\mathbf{Y}}\right)^{-1} = \sigma^2 \mathbf{W}\hat{\mathbf{Y}}\boldsymbol{\varepsilon}, \text{ with } \boldsymbol{\varepsilon} \equiv \sigma^2\left(\hat{\mathbf{Y}}^T\hat{\mathbf{Y}}\right)^{-1} . \tag{27 and 28}$$

$$\left(\frac{\partial b_j}{\partial W_n}\right) = \frac{1}{\sigma^2}\sum_{k=0}^{M}\varepsilon_{jk}Y_k\left(\boldsymbol{\rho}_n\right) . \tag{29}$$

Substituting Eq. (28) into Eq. (26), the expression for the uncertainties reduces considerably:

$$\sigma_{b_j}^2 = \frac{1}{\sigma^2}\sum_{k=0}^{M}\sum_{m=0}^{M}\varepsilon_{jk}\varepsilon_{jm}\sum_{n=1}^{N}Y_k\left(\boldsymbol{\rho}_n\right)Y_m\left(\boldsymbol{\rho}_n\right) = \sum_{k=0}^{M}\sum_{m=0}^{M}\varepsilon_{jk}\varepsilon_{jm}\alpha_{km} . \tag{30}$$

Recalling the definition of the curvature matrix $\boldsymbol{\alpha}$ for the basis $\{\mathbf{Y}_j\}$,

$$\boldsymbol{\alpha} \equiv \frac{1}{\sigma^2}\left(\hat{\mathbf{Y}}^T\hat{\mathbf{Y}}\right), \tag{31}$$

and the fact that the error matrix $\boldsymbol{\varepsilon}$ is the inverse of $\boldsymbol{\alpha}$,

$$\sigma_{b_j}^2 = \sum_{k=0}^{M}\varepsilon_{jk}\sum_{m=0}^{M}\varepsilon_{jm}\alpha_{km} = \sum_{k=0}^{M}\varepsilon_{jk}\delta_{jk} = \varepsilon_{jj} , \tag{32}$$

$$\sigma_{b_j}^2 = \varepsilon_{jj} \equiv \sigma^2 \left[\left(\hat{\mathbf{Y}}^T \hat{\mathbf{Y}} \right)^{-1} \right]_{jj} . \tag{33}$$

When the measurement uncertainty σ of each point is unknown, it may be estimated from the variance of the fit (Bevington 1969:154) as follows.

$$\sigma_n^2 \approx \sigma^2 \approx s^2 \equiv \frac{1}{N - M - 1} \left\| \mathbf{W}' - \mathbf{W} \right\|^2 . \tag{34}$$

As before, N is the number of points in the measurement domain, (M+1) is the number of parameters used in the fit, and $\mathbf{W}'$ is the wavefront fit reconstructed from the coefficient vector $\mathbf{b}$. Combining Eqns. (33) and (34), the estimated uncertainty in an individual fit coefficient b_j is

$$\sigma_{b_j}^2 = \varepsilon_{jj} = \frac{\left\| \mathbf{W}' - \mathbf{W} \right\|^2}{N - M - 1} \left[\left(\hat{\mathbf{Y}}^T \hat{\mathbf{Y}} \right)^{-1} \right]_{jj} . \tag{35}$$

Up to this point, the orthogonality of the polynomial basis has not been considered; thus the error estimation method up through Equation (34) is generally applicable to any polynomial basis and any set of fit coefficients. When $\{\mathbf{Y}_j\}$ *is* an orthogonal basis, then the curvature matrix $\boldsymbol{\alpha}$ and its inverse the error matrix $\boldsymbol{\varepsilon}$ are both diagonal, making the matrix inversion trivial. Equation (33) reduces to these equivalent expressions.

$$\sigma_{b_j}^2 = \varepsilon_{jj} = \frac{\sigma^2}{\mathbf{Y}_j \mathbf{Y}_j^T} = \frac{\sigma^2}{\left\| \mathbf{Y}_j \right\|^2} = \frac{1}{N - M - 1} \frac{\left\| \mathbf{W}' - \mathbf{W} \right\|^2}{\left\| \mathbf{Y}_j \right\|^2} = \frac{1}{N - M - 1} \frac{\left\| \mathbf{b} \hat{\mathbf{Y}}^T - \mathbf{W} \right\|^2}{\left\| \mathbf{Y}_j \right\|^2} . \tag{36}$$

Here, the estimated uncertainties in the fit coefficients of the orthogonal basis polynomials are easily calculated. However, the orthogonal basis $\{\mathbf{Y}_j\}$ is often used only as an intermediate step in the calculation of the fit coefficients of the more convenient basis $\{\mathbf{X}_j\}$, from which the orthogonal basis was calculated. Since the transformation between the two bases is known, calculation of the estimated uncertainties in the original basis coefficients is very straightforward. $\mathbf{G}$ is determined during the calculation of the orthogonal basis. From the definition of $\mathbf{G}$, Eq. (19a),

$$\mathbf{c} = \mathbf{b} \mathbf{G} \quad \Rightarrow \quad c_j = \sum_{k=0}^{M} b_k G_{jk} . \tag{37}$$

Using the method of error propagation and the fact that $\mathbf{G}$ has no dependence on the measured wavefront,

$$\sigma_{c_j}^2 = \sum_{k=0}^{M} \sigma_{b_k}^2 \left(\frac{\partial c_j}{\partial b_k} \right)^2 = \sum_{k=0}^{M} \sigma_{b_k}^2 G_{jk}^2 . \tag{38}$$

From Eq. (10) $\sigma_{b_k}^2$ is known in terms of $\{\mathbf{Y}_j\}$. This is easily converted to $\{\mathbf{X}_j\}$:

$$\sigma_{c_j}^2 = \sigma^2 \sum_{k=0}^{M} \frac{G_{jk}^2}{\left\| \mathbf{Y}_k \right\|^2} = \sigma^2 \sum_{k=0}^{M} \frac{G_{jk}^2}{\left\| [G]_{\text{row } k} \hat{\mathbf{X}}^T \right\|^2} = \sigma^2 \sum_{k=0}^{M} \frac{G_{jk}^2}{\left\| \sum_{l=0}^{M} G_{lk} \mathbf{X}_l \right\|^2} . \tag{39}$$

From this expression, the uncertainties in the fitting coefficients of the convenient basis are easily calculated.